Anode defects' propagation in Polymer Electrolyte Membrane Fuel Cells

Salah Touhami, Marie Crouillere, Julia Mainka, Jérôme Dillet, Christine Nayoze-Coynel, Corine Bas, Laetitia Dubau, Assma El Kaddouri, Florence Dubelley, Fabrice Micoud, et al.

▶ **To cite this version:**

Salah Touhami, Marie Crouillere, Julia Mainka, Jérôme Dillet, Christine Nayoze-Coynel, et al.. Anode defects' propagation in Polymer Electrolyte Membrane Fuel Cells. Journal of Power Sources, 2022, 520, pp.230880. 10.1016/j.jpowsour.2021.230880 . hal-03476636

HAL Id: hal-03476636
https://hal.science/hal-03476636v1

Submitted on 13 Dec 2021

HAL is a multi-disciplinary open access archive for the deposit and dissemination of scientific research documents, whether they are published or not. The documents may come from teaching and research institutions in France or abroad, or from public or private research centers.

L'archive ouverte pluridisciplinaire **HAL**, est destinée au dépôt et à la diffusion de documents scientifiques de niveau recherche, publiés ou non, émanant des établissements d'enseignement et de recherche français ou étrangers, des laboratoires publics ou privés.

Distributed under a Creative Commons Attribution - NonCommercial - NoDerivatives 4.0 International License

Anode defects' propagation in Polymer Electrolyte Membrane Fuel Cells

Salah Touhami (1), Marie Crouillere (2), Julia Mainka (1), Jérôme Dillet (1), Christine Nayoze-Coynel (3), Corine Bas (2), Laetitia Dubau (2), Assma El Kaddouri (1), Florence Dubelley (2), Fabrice Micoud (3), Marian Chatenet (2), Yann Bultel (2), Olivier Lottin (1)

(1) Univ. Lorraine, CNRS, LEMTA, 54500 Vandœuvre-lès-Nancy, France

(2) Univ. Grenoble Alpes, Univ. Savoie-Mont Blanc, CNRS, Grenoble INP, LEPMI, 38000 Grenoble, France

(3) Univ. Grenoble Alpes, CEA, LITEN, F-38054 Grenoble, France

Abstract

Defects-propagation in polymer electrolyte membrane fuel cells membrane electrode assemblies (MEA) is investigated via Accelerated Stress Tests (AST) combining load (hence potential) and load-driven humidity cycling, and open-circuit voltage. Customized MEA with lack of anode catalyst layer at two different locations -near the hydrogen inlet or outlet- are fabricated and subjected to the AST. Periodical electrochemical characterizations are performed using a segmented cell, enabling to track the cell performance and anode/cathode electrochemical surface area (ECSA) over the test period with a spatial resolution along the gas channels. These observations are completed by *post mortem* analyses of the MEA.

The MEA accelerated degradation is obvious, with multiple impacts on the cell performance and materials. More specifically, the results brought first evidence of defects propagation, in term of anode ECSA loss, in the direction of the hydrogen flow. The cathode ECSA is also impacted, although seemingly homogeneously. Significant membrane thinning is observed for the defective segments, without propagation to the adjacent ones. Anode and cathode local potential monitoring during the AST reveals the absence of cathode high-potential excursion, in both the segments with/without initial defects: the membrane and anode accelerated degradation is governed by chemical mechanisms like gas crossover rather than electrochemical mechanisms induced by high-potential excursions.

Highlights

- Anode active surface defects propagate in the direction of the hydrogen flow.
- The cathode active surface is also impacted, but homogeneously.
- Anode active surface defects entail significant membrane thinning.
- Membrane thinning is likely governed mainly by chemical mechanisms.

Introduction

Defects known to shorten the lifetime of polymer electrolyte membrane fuel cells (PEMFC) can appear on different membrane electrode assembly (MEA) components and under different forms due to manufacturing processes or operational aging of the fuel cell (FC) [1–6]. The degradation of catalyst layers (CL) is one of the main factors that impacts the FC lifetime. The degradation of the CL occurs mostly at the cathode, rather than the anode, due to higher local potentials [7–9], leading to carbon corrosion (which can induce Pt particles detachment), Pt migration (leading to Pt particle agglomeration and coalescence) and Pt dissolution and growth due to redeposition of Pt ionic species [9–13]. These degradation mechanisms strongly depends on the operating conditions: high temperature and relative humidity (RH) are generally considered as aggravating factors for degradation [14–19]. However, although most of the works focus on the cathode, strong degradation at the anode was also evidenced under specific conditions, such as start-up and shut-down cycling, wet-dry cycling, potential cycling, and anode flooding [20–23]. Many studies have also shown that the use of reformed hydrogen containing varying amounts of carbon monoxide (CO) has a harmful effect on the anode [21,24–28], the damages being often reversible.

The possible impact of such anode CL -reversible or irreversible- degradation on the other MEA components has very rarely been studied, although this electrode plays a key role in keeping the cathode local potentials low: this was widely attested by the many studies related to fuel starvation, whether this phenomenon is induced by FC start-up and shut-down [29–34] or more common operating conditions like the slow water accumulation in the hydrogen flow-field with a dead-ended anode [35,36]. In addition, and according to Sompali et al. [37], the cathode overlap -occurring in the MEA perimeter regions when the anode CL area is smaller than that of the cathode- may lead to so-called "*open circuit voltage (OCV) conditions*" and to accelerated membrane degradation. Although local membrane degradation was clearly attested in such conditions, local potentials were not -to the best of our knowledge- measured,

but instead (and at best) numerically simulated by Sompali et al. [37] or other authors they mentioned [38,39]. Therefore, the exact mechanisms at stake may not be fully understood yet. Nevertheless, such membrane degradations in the regions where the cathode overlaps the anode were also confirmed by Ohma et al. [40] in OCV conditions. For these reasons, it is reasonable to suspect that similar degradation mechanisms may occur anywhere in the cell when the anode CL is missing (due to possible imperfect manufacturing processes) or when it is strongly degraded; all the more so since anode defects or anode degradation have only a small impact on FC performances [22], so that they can remain undetected for rather long durations.

In addition to the CL, the membrane is also subjected to high mechanical and chemical stresses during FC operation [41–47]. The mechanical stresses are mainly due to humidity cycling, that causes the swelling and shrinking of the membrane following water-content variations. These stresses can generate mechanical fatigue and lead to the formation and/or growth of cracks or tears [43,48]. The chemical stresses are mainly due to the action of oxygen ($OOH\bullet$ and $HO\bullet$) and hydrogen ($H\bullet$) radicals on the ionomer chemical structure [45,49–53]. It is commonly admitted that these radicals are generated by the decomposition of hydrogen peroxide (H_2O_2). There are however some controversies regarding the origin of H_2O_2, that can appear either on the cathode or on the anode side and result from either electrochemical or chemical reaction [49,51,54–59]. Finally, it is also well-known that OCV, low RH and high temperature lead to accelerated membrane thinning [40,60,61]. Numerous studies have been conducted in the literature to better understand the membrane degradation mechanisms under chemical, mechanical, or combined chemical/mechanical stresses, through *in situ* [42,43,50,54,62–64] or *ex situ* [44,46,65–67] experiments.

In addition to mechanical, chemical, and electrochemical degradation, CL and membrane defects can also be due to imperfect MEA manufacturing processes. They can take many forms: cracks, surface roughness, delamination, or thickness variations in the case of CL [4,68–72] and pinholes, cracks, cuts, abrasions, tears, air bubbles and foreign matter inclusions in the case of membranes [2,73–76]. It must be emphasized that the current trend to significantly lower catalyst loading at the cathode and - even more so - at the anode makes the risk of a local lack of CL more likely [6,76].

The possible propagation of such defects from their original position to the rest of the active area or to other components is poorly understood and has been barely studied in the literature. Among the few works published, Uchiyama et al. [77] studied CL crack formation by bulge deformation under humidity cycles using experiments and finite-element numerical simulations. Zhao et al. [69] observed (through *ex situ* experiments) microstructure changes of the CL under wet-dry cycles: a considerable growth of the catalyst agglomerates, together with the formation of cracks and pinholes was highlighted. These changes of the microstructure in the CL led to an irreversible loss of the ElectroChemical Surface Area (ECSA), catalytic activity, and performance. Chang et al. [70] investigated the effects of RH and/or thermal cycles on the structural changes of CL through *ex situ* experiments: humidity cycling plays a more important role in cracks propagation and growth than temperature cycling. Philips et al. [78] used a segmented-cell to understand how local lacks of active layer ranging from 0.125 to 1 cm^2 at the cathode of a 50 cm^2 cell impacted the performance, in wet and dry conditions: with 0.5 and 1 cm^2 defects, slight voltage drops were observed under dry operation and high current densities, while the impact of 0.25 cm^2 irregularities was detected only through modifications in the local currents distribution. Tavassoli et al. [79] analyzed the effect of CL defects on local membrane degradation in PEMFC in operation: cracks in the anode and cathode CL had a negligible impact on membrane degradation unlike anode CL delamination, which can accelerate local membrane thinning. Cathode delamination had no apparent effect.

As a summary, these studies seem to show that the propagation of defects may indeed occur, either to the membrane and/or to the CL. However, and to the best of our knowledge, the occurrence of a spatial propagation of MEA defects within a cell, *i.e*. from one region of the flow field to another, has never been clearly evidenced yet.

In this work, we studied the impact and possible propagation of anode defects taking the form of a lack of anode CL. To that goal, not knowing a priori which component would be impacted by the anode defects, we applied an Accelerated Stress Test (AST) that was designed to stress the electrodes and the membrane: the FC temperature was set to 80°C and material degradations were induced or exacerbated thanks to the combination of load (and thus potential) cycling (between 0, 0.25 and 1.3 A/cm^2), load-driven RH cycling and OCV.

The customized MEA were intentionally prepared with anode defects close to the hydrogen inlet or outlet. The measurements were performed using a segmented and instrumented cell, making it possible to follow the evolution of the local performances, *i.e*. currents and electrode potentials, as well as monitor the MEA aging, through the measurement (every 24 hours) of local ECSA and impedance. Then, the results were compared to those of reference MEA, without defects.

Experimental setup and Materials

Segmented linear cell

This work was carried out using a segmented linear cell (Fig. 1) of 30 cm² active area (30 × 1 cm²) with 5 straight and parallel gas-distribution channels (30 cm long, 1 mm wide and 0.7 mm deep) on both anode and cathode sides. The channels are spaced 1 mm apart from each other. The cell is made of 316L stainless steel coated with a thin gold layer to lower the electrical contact resistance with the gas diffusion layers. The distributor plate on the cathode side is made up of 20 segments (1.5 cm × 1 cm each) electrically insulated along the channel length, which allows individual current collection on each of them. The segments are held together with a layer of Epoxy resin. The anode side is not segmented. The cell is also equipped with an independent and segmented auxiliary channel on the cathode side. This channel is parallel to the air channels and feeds local Reference Hydrogen Electrodes (RHE) with 50% HR H_2, allowing the measurement of local anode and cathode potentials. The heating/cooling water circuit passes through the end-plates holding and clamping the anode and cathode flow-field plates.

Although much information regarding the overall cell architecture and the measurement of the potentials is available in references [35,36,80], it may be useful to discuss in more detail the meaning of the electrode potentials in the presence of anode defects in the form of a lack of CL. Fig. 1 shows how they were measured thanks to a cross-sectional view of the segmented cell, with V_m^a standing for the metal potential in the anode, while V_m^c is the metal potential of the cathode. Both are assumed uniform along the gas channels (*i.e*. at every location of the flow-field) because of the high electronic conductivity of the electrodes, Gas Diffusion Layers (GDL) and plates. V_m^a and V_m^c can be directly and easily measured at the cell terminals and their difference equals the cell voltage: $U = V_m^c - V_m^a$. In electrochemistry, electrode potentials are

defined as the difference between the metal potential and the electrolyte potential, so that the anode and cathode potentials in Fig.1, $V^a(i)$ and $V^c(i)$ can be expressed as:

$$V^a(i) = V_m^a - V_e(i) \quad (1)$$

and,

$$V^c(i) = V_m^c - V_e(i) \quad (2)$$

with $V_e(i)$ the electrolyte potential.

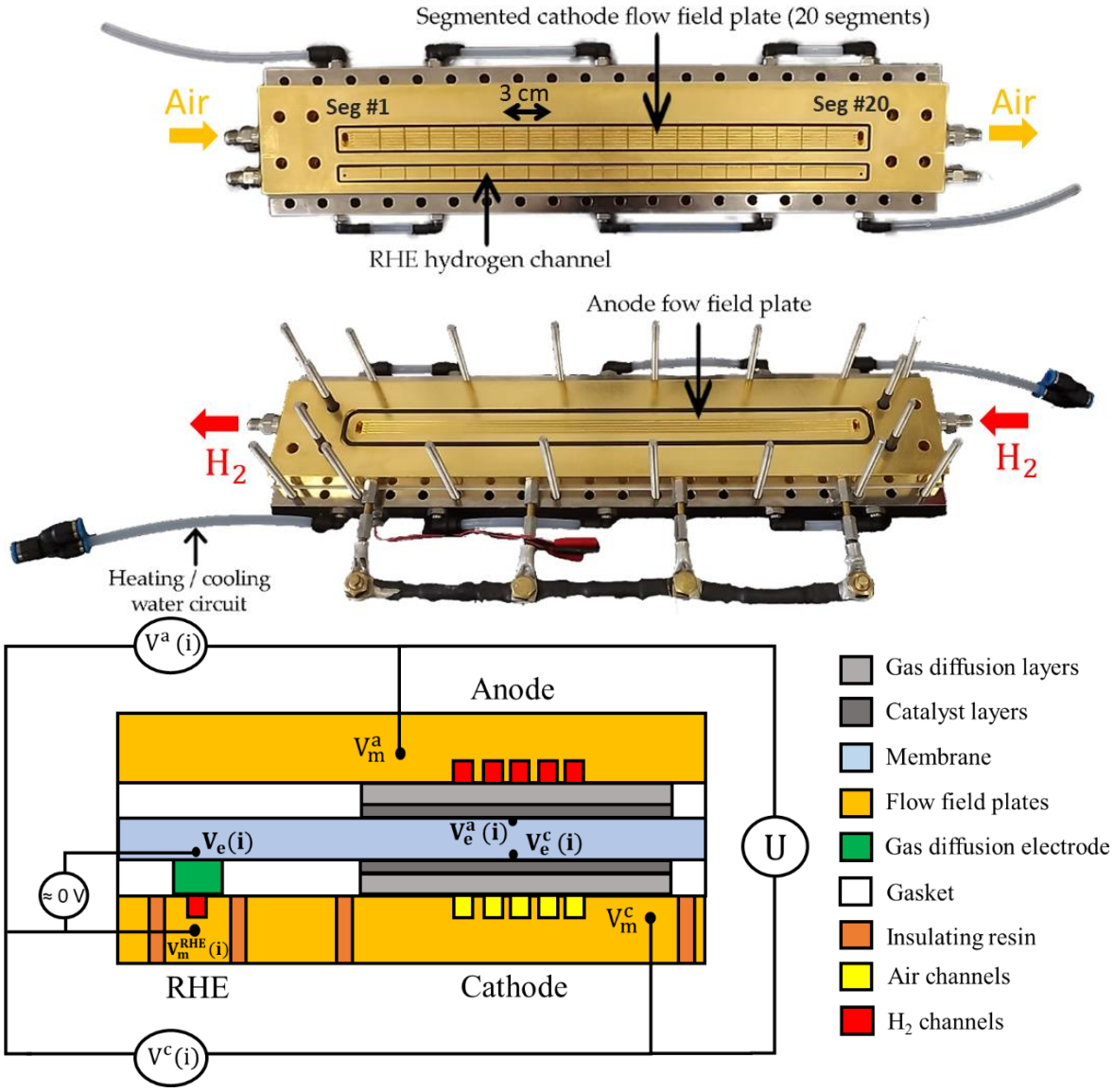

Figure 1. Pictures and operation principle of the linear segmented cell. Up: segmented cathode flow-field with the auxiliary hydrogen channel feeding the RHE used to measure the local potentials. Middle: anode flow-field plate. Bottom: cross-sectional view of the cell. The reference electrodes give access to the local electrolyte potential $V^e(i)$ and thus to the anode and cathode potentials of each segment [22,35].

Contrary to V_m^a and V_m^c, $V_e$cannot be assumed uniform along the gas channel due to non-negligible membrane ionic resistance in the plane directions, even in perfectly-humidified conditions. Thus $V_e(i)$ stands for the local electrolyte potential in segment #i, and $V^a(i)$ and $V^c(i)$ are thus the *local* anode and cathode potentials, assuming that there is no significant variation of $V_e(i)$ over a single segment, which is reasonable regarding their small active area: one twentieth of the total cell area, *i.e*. 1.5 cm². Note that there is also a slight variation of the membrane potential through its thickness, depending on the current density. It would therefore be more accurate to use $V_e^a(i)$ and $V_e^c(i)$ in equations (1) and (2), designating the electrolyte potential at the anode or cathode interface. However, the difference between $V_e^a(i)$ and $V_e^c(i)$ is rather low so that it can be neglected in most of the cases: $V_e^a(i) - V_e^c(i) = r_e(i) \times i$, with $r_e(i)$ the membrane resistance in segment #i and i the current density, is of the order of 10 mV with a fully-hydrated 18 µm thick membrane of 0.1 S/cm and a current density of 0.5 A/cm².

The lack of anode CL corresponds to a very specific situation that is discussed in the last part of the paper. As illustrated in Fig. 1, $V_e(i)$ is measured thanks to the twenty Reference Hydrogen Electrodes (RHE) located along the hydrogen auxiliary channel on the cathode side. The local RHE were made from 0.3 $mg_{Pt}.cm^{-2}$ SGL 29BC Gas Diffusion Electrodes (GDE) that were cut into 5 mm disks and placed onto the membrane, about 1.3 cm away from the cathode.

The local anode potential $V^a(i)$ are thus given by $V_m^a - V_m^{RHE}(i)$, assuming $V_m^{RHE}(i) \approx V_e(i)$. It is important to keep in mind that this measurement can be performed independently of the presence of the anode CL; although strictly speaking the result cannot be called an anode potential when there is locally no anode. The cathode potentials are determined using the same approach: $V^c(i) = V_m^c - V_m^{RHE}(i)$.

MEA fabrication

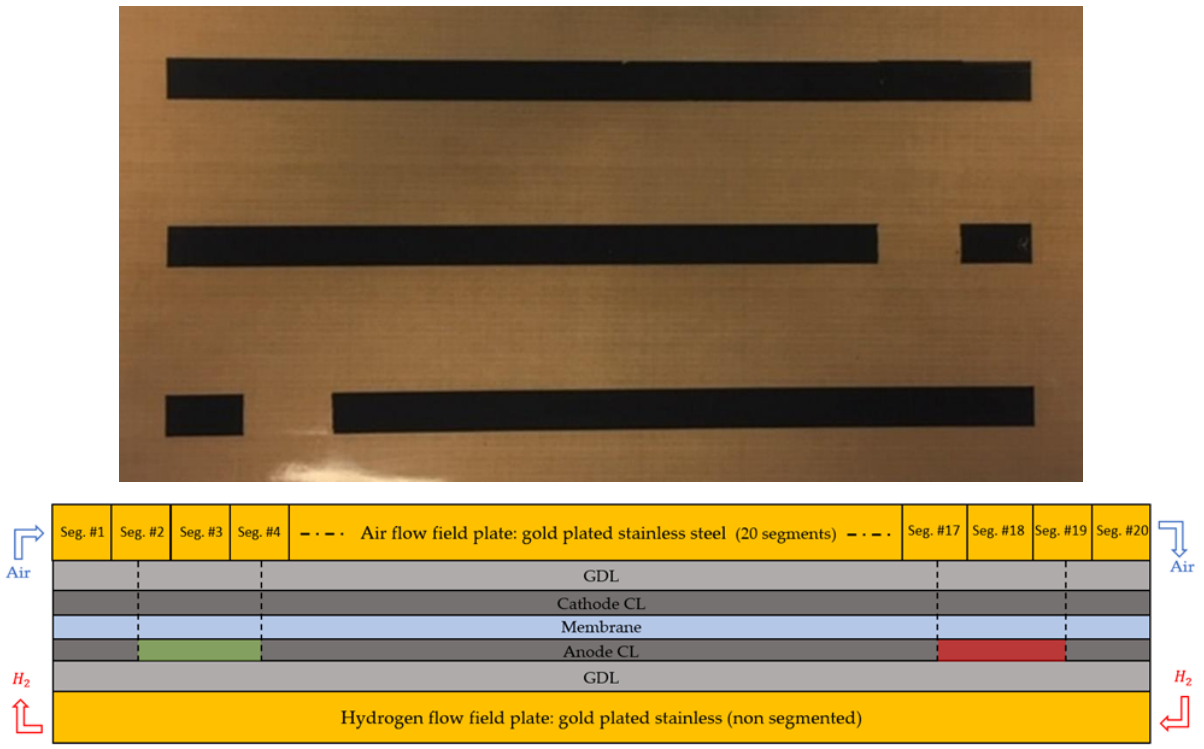

Figure 2. Up: anode -before transfer on the membrane- with -or without- a lack of CL at one end. Below: longitudinal sectional view of the segmented cell. The location of the defect is situated either at the anode inlet (in green) or outlet (in red).

The MEA were made with reinforced Gore 735.18 membranes, 50wt% Pt/C Vulcan XC-72 (Tanaka TEC10V50E) at the cathode, and 30wt% Pt/C graphitized High Surface Area (HSA) carbon (Tanaka TEC10EA30E-HT) at the anode. The Pt loadings were 0.1 $mg_{Pt}.cm^{-2}$ for the anode and 0.2-0.3 $mg_{Pt}.cm^{-2}$ for the cathode. The GDL were 220 µm-thick Freudenberg H23C7, compressed to 175 µm. The thickness was controlled using 150 µm thick PTFE gaskets on each side, in addition to the 25 µm thick reinforcement layers framing the membrane around the CL -on the anode and cathode sides- to protect it against premature rupture. As illustrated in Fig. 2, defects have an area of 3 cm^2, corresponding to the complete area of segment #3 and half of area of segments #2 and #4 (when close to the hydrogen outlet) or to the whole area of segment #18 and half of that of segments #17 and #19 (when close to the hydrogen inlet). This quite large defect area, *i.e.* 10% of the total MEA area, has been chosen following the results of Philips et al.[78], who showed that a 2% defect area had only a slight impact on the performance. The electrodes have been made by bar-coating using a frame of appropriate thickness to reach the desired catalyst loading. The Catalyst Coated Membranes (CCM) were manufactured by decal transfer of the electrodes onto the membrane; both electrodes were transferred simultaneously.

Operating Conditions and Accelerated Stress Test

The cell was fed with air and hydrogen in counter-flow: segment #1 corresponds to the air inlet at the cathode and H_2 outlet at the anode, while segment #20 corresponds to the air outlet at the cathode and H_2 inlet at the anode. The temperature of the flow-field plates was maintained at 80°C. The outlet pressure was set to 1.5 bar (absolute). on both sides and the RH of gases (air, hydrogen, and nitrogen) was set to 50% at the FC inlet. The cell pressure was controlled at the exit of the electrode compartments thanks to pressure regulators installed downstream of the water condensers and membrane dryers used to remove water from the air and hydrogen exiting the cathode and anode compartments.

Nitrogen (50% RH) was introduced into the anode or cathode compartment to measure the hydrogen permeation current as well as the ECSA, while the opposite electrode was fed with hydrogen, acting thus as a counter and reference electrode. The measurement protocol consisted in first flushing the flow-field plates, with nitrogen on one side and hydrogen on the other side, for ten minutes, before measuring the hydrogen permeation current at 0.6 V. Then the nitrogen flow was stopped and the ECSA was measured by cycling the voltage between the working and the counter/reference electrode, between 0.1 and 0.8 V, at a sweep rate of 50 mV s^{-1}. The hydrogen permeation current was measured on both the anode and cathode sides to check the repeatability of the results.

In regular operating conditions (*i.e.* aging test and acquisition of the impedance spectra or of the polarization curves), the FC -overall- current intensity was imposed by the electronic load (Armel 0–100A/0-10 V). The local currents produced by the 20 segments were measured with a home-made electronic card, using the potential drop at the terminals of 5 mΩ shunt resistances and a x600 amplification gain.

When voltammograms and hydrogen permeation currents were recorded, the cell was automatically connected to a bipolar power source (Kikusui PBZ-20-20A) to impose positive and negative voltage. A supplementary 5 mΩ shunt resistance was used to get the FC overall current, while the local currents were measured with the same electronic card as in normal operation.

Before the AST, each new MEA was subjected to a two-hour break-in stage, consisting in the repetition of potentiostatic steps at OCV (30 s), 0.6 V (45 s) and 0.3 V (60 s).

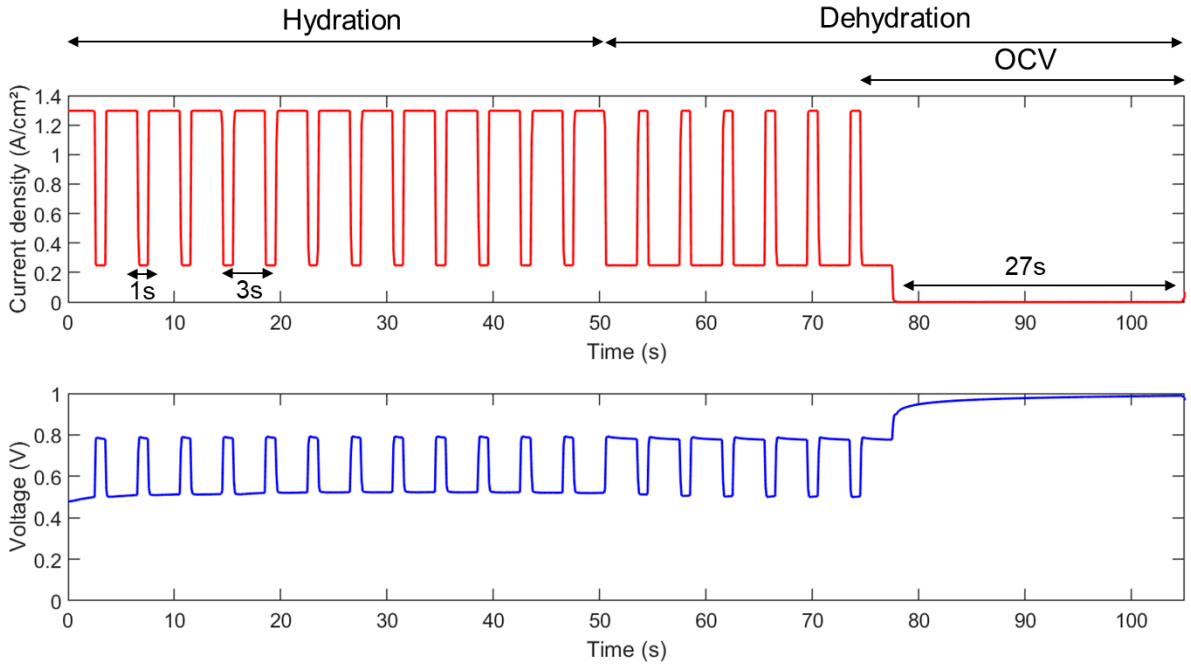

Figure 3. Current density and voltage profiles during the RH and load cycling AST. The hydration stage consists of alternating 1 s at low current (0.25 A/cm²) and 3 s at high current (1.3 A/cm²) sequences and lasts 52 s. The dehydration stage consists of alternated sequences of 3 s at low current and 1 s at high current, followed by 27 s at OCV (total duration = 105 s) [22].

As mentioned above, the accelerated aging protocol was designed to impact the CL and the membrane by combining load cycling, OCV hold, and load-driven humidity cycling. The principle of such combined-stressor AST consists of keeping the gas flow rates constant, and their humidity to a low or medium value [22,42,81,82]. In our case, the gases were slightly humidified (50% RH) and their flow rates did correspond to hydrogen and air stoichiometries of 1.5 and 2, respectively, at the highest current density (1.3 A/cm²). Thus, the stoichiometries increased to 7.8 and 10.4 when the current density was lowered to 0.25 A/cm² and, of course, to infinite values during the 27 seconds OCV hold at the end of each sequence. Fig. 3, shows the whole of the 105 seconds AST sequence, consisting in a 52 s hydration stage (with an alternation of 1 s at low current and 3 s at high current, followed by a dehydration stage (3 s at low current and 1 s at high current) including a 27 second OCV hold step. This AST has been used in one of our previous works [22] with other MEA because of its ability to combine, in addition to potential cycling, a membrane chemical stress during OCV hold (through the formation of hydrogen peroxide), and a mechanical stress via the humidity cycling.

At Beginning of Life (BoL), the FC voltage reached *ca*. 0.8 V at 0.25 A/cm² and 0.5 V at 1.3 A/cm², these values are slightly varying depending on the MEA tested and on the presence (or absence) of defects. The AST sequence was repeated during ten days, with a characterization stage performed every 24 hours to monitor the possible decrease of the FC performance and materials degradation. This characterization stage included:

1. 30 min operation at a constant current density of 0.5 A/cm²,
2. measurement of the local and global impedance spectra, using a peak-to-peak perturbation amplitude of 50 mA, with frequencies ranging from 20 mHz to 10 kHz,
3. measurement of the polarization curves according to the protocol described in [22],
4. and measurement of the hydrogen permeation current and electrode ECSA, on both the anode and cathode sides, as described above.

Results

Segmented cell: impact of a lack of anode active layer on voltage decay and hydrogen permeation current

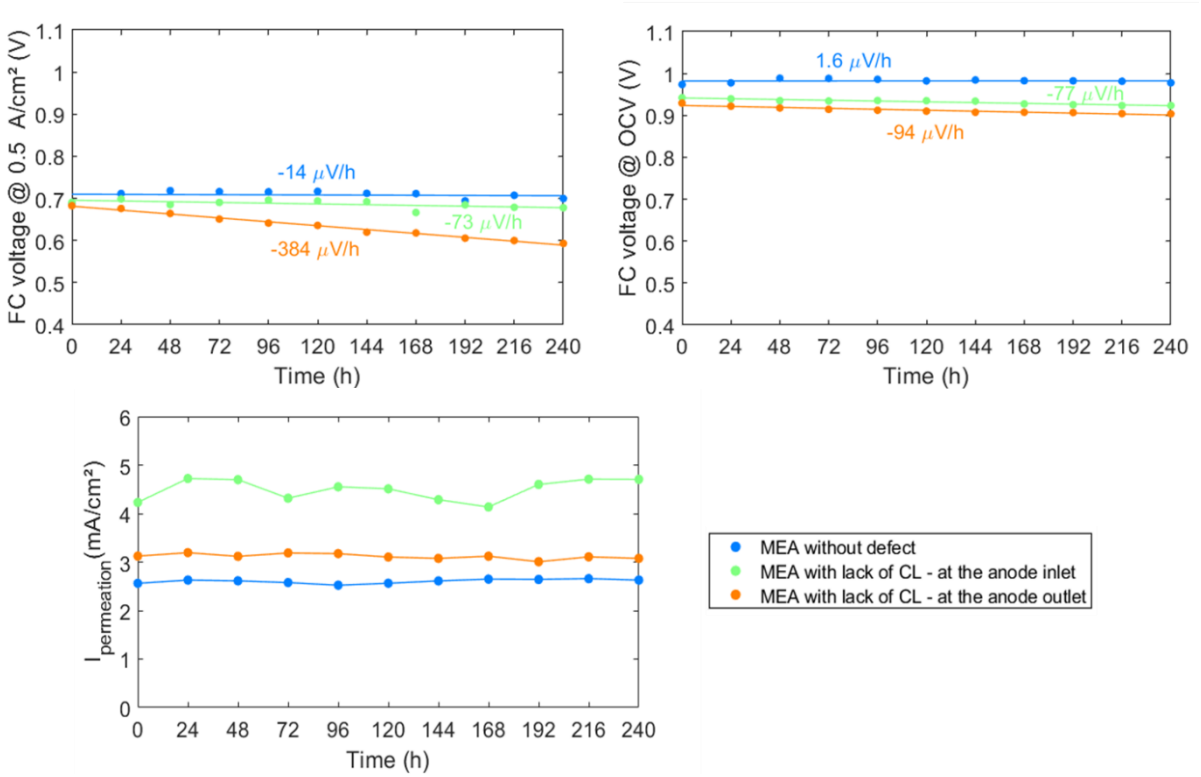

Figure 4. Variation of the FC voltage at 0.5 A/cm² (top, left), of the OCV (top, right) and of the hydrogen permeation current (bottom) during AST performed with a reference MEA (without defect), a MEA with a lack of anode CL close to the hydrogen inlet, and a MEA with a lack of anode CL close to the hydrogen outlet. All data were measured during the characterization stage performed every 24 h. The voltage degradation rates were estimated using a linear interpolation of the dots.

The variations of the overall cell voltage at 0.5 A/cm² and OCV during the AST are given in Fig. 4 (top) in the case of three different MEA:

- a MEA without defect as homogeneous reference MEA,
- a MEA with a lack of anode CL close to the hydrogen inlet,
- a MEA with a lack of anode CL close to the hydrogen outlet.

Fig. 4 (top, left) shows that the MEA with a lack of anode CL are subjected to much larger performance degradation rates at 0.5 A/cm² than the homogeneous reference MEA. This trend seems to depend much on the location of the defect: -384 µV/h when it is close to the hydrogen outlet, *vs*. -73 µV/h when it is close to the hydrogen inlet. On the other hand, the performance degradation rate of the MEA without defect was only of -14 µV/h. The same conclusions can be drawn from the evolutions of the OCV in Fig. 4 (top, right), with a degradation rate of -94 µV/h when the defect is close to the hydrogen outlet, and of -77 µV/h when it is close to the hydrogen inlet. In contrast, the MEA without defect showed no clear change of its OCV over a test duration of 240 hours: the voltage increased slightly during the first 48 hours and then decreased at a relatively slow rate, *i.e*. -49 µV/h; this gives a slight OCV increase of 1.6 µV/h on the whole test duration.

Fig. 4 (bottom) also shows the change of the hydrogen permeation currents during the AST. As mentioned above, the hydrogen permeation currents were measured on the anode and the cathode side during the characterization stage performed every 24 hours: no significant difference being observed between both sides, only the average values are plotted for clarity. First, in all cases, the hydrogen permeation currents remained constant during the AST: the possible premature degradation of the membrane in the absence of anode CL did not lead to its failure, or imminent failure.

Segmented cell: changes of the local anode and cathode ECSA

To put forward a possible propagation of the defects along the anode or cathode CL, Fig. 5 shows the variation of the local anode and cathode ECSA during the AST:

- The reference MEA without defect, *i.e*. with homogeneous anode and cathode CL in Fig. 5a (cathode) and Fig. 5b (anode).

- The MEA with a lack of anode CL near the hydrogen outlet in Fig. 5c (cathode) and Fig. 5d (anode).
- And the MEA with a lack of anode CL near the hydrogen inlet in Fig. 5e (cathode) and Fig. 5f (anode).

In addition, Table 1 gives the variation of the average anode and cathode ECSA between their BoL and the EoT.

For the homogeneous MEA, the local ECSA at the cathode (Fig. 5a) strongly degrades (overall loss of 34%, Table 1), while (Fig. 5b) a slight homogenous increase is observed at the anode (overall gain of 20%, Table 1). These variations were rather homogeneous at both electrodes, *i.e*. no segment or region of the MEA seemed to behave differently compared to the others. In the same way, the cathode ECSA of the MEA with a lack of CL showed a severe (overall loss of about 40%, Table 1) and seemingly homogeneous degradation, whatever the defect location, close to the anode outlet (Fig. 5c) or inlet (Fig. 5e). However, it must be kept in mind that measuring the cathode ECSA in segments #2, #3 and #4 (when the defect is close to the hydrogen outlet) or segments #17, #18 and #19 (when the defect is close to the hydrogen inlet) is uncertain, due to the absence of the anode CL acting as a counter electrode.

Table 1. Beginning of Life (BoL) and Enf of Test (EoT) average anode and cathode ECSA of the MEA without defect, the MEA with a lack of CL close to the anode outlet, and the MEA with a lack of CL close to the anode inlet.

MEA		Cathode				Anode		
	BoL ECSA (m^2/g)	EoT ECSA (m^2/g)	Loss (%)		BoL ECSA (m^2/g)	EoT ECSA (m^2/g)	Loss (%)
Without defect	63	41	-34		38	46	+21 (gain)
With a lack of CL at the anode inlet	60	34	-43		55	45	-18
With a lack of CL at the anode outlet	48	29	-40		40	38	-5

In contrast, a rather different evolution of the local anode ECSA was observed in the MEA with defects compared to the homogeneous MEA:

- The MEA with a lack of the anode CL close to the anode outlet (Fig. 5d) experienced a global 10% increase of the anode ECSA during the first 96 hours and a slight degradation afterward so that the initial and end of test values were close to each other

(-5% in Table 1). However, segment #1 (*i.e*. downstream from the defect in the direction of the hydrogen flow) did not show the same behavior, with a strong decrease of ECSA.

- The variation of the anode local ECSA was quite heterogeneous in the MEA with the defect located close to the anode inlet (Fig. 5f), with a significant degradation in the segments that were located downstream, and close to the defect (from #16 to #10). The local ECSA degradation rates seem less pronounced as one moves away from the defect in the direction of hydrogen flow. In addition, no significant degradation of the anode ECSA was observed upstream of the defect (segment #20). Overall, the degradation of the average anode ECSA over the test duration reaches 18% (Table 1).

These results suggest that, in term of ECSA, the anode defect may propagate along the anode CL in the direction of hydrogen flow.

Membrane microscopy analyses

As a complement to the monitoring of the local ECSA, the possible variation of the membrane thickness was also assessed by *post mortem* optical microscopy analyses. Different segments were embedded in epoxy resin to observe the membrane: Fig. 6 presents its overall thickness in these segments at the end of the 240 hours AST. For comparison, the thickness of pristine Gore 735.18 membranes is 18 µm. These measurements were performed for the three MEA: homogeneous (left), with a lack of anode CL near the hydrogen outlet (middle) and near the hydrogen inlet (right), and for few segments distributed along the cell. Ten measurements were made in the segments with a defect, *i.e*. five in the channel region and five below the land. Only three measurements were made in the other “regular” segments because it quickly appeared that the membrane thickness was unaffected. The results revealed a *ca*. 25% decrease in membrane thickness in the segment with the defect (*i.e*. #3 or #18) while no thinning of the membrane was evidenced in the other segments, including the adjacent ones. These results are not fully consistent with those discussed above, because a propagation of the defect in the direction of the hydrogen flow was observed when considering the anode CL ECSA. Nevertheless, one cannot exclude that performing the AST for longer duration would eventually lead to a non-negligible thinning of the membrane in the adjacent segments, or even further along the hydrogen channels: complementary tests are under way to clarify this point.

As a complement, Figure 7 shows the average thickness of the membrane measured at EoT, below the channels and below the lands in the segments with a lack of anode CL (*i.e*. #3 and #18). As mentioned earlier, five measurements were made in each case and only the average values and the standard deviations are plotted.

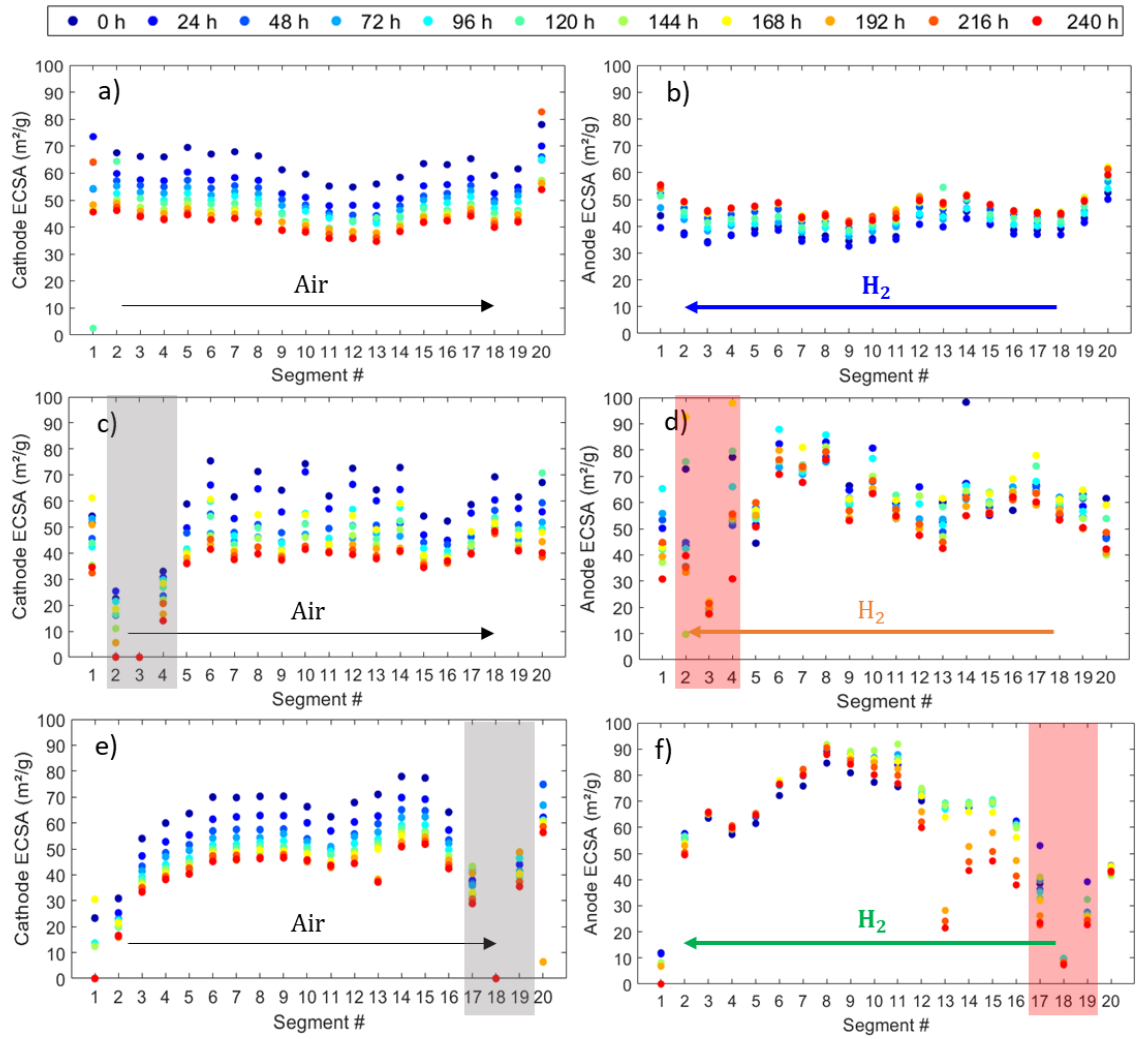

Figure 5. Variation of the local ECSA during the AST at the cathode (a, c and e) and the anode (b, d and f) in the case of the MEA without defect (a and b), the MEA with a lack of CL close to the anode outlet (c and d) and the MEA with a lack of CL close to the anode inlet (e and f), respectively. The segments corresponding to the anode defects are marked in red (d and f). The segments marked in grey are those where the cathode ECSA measurements cannot be considered as reliable due to the absence of a counter electrode.

Fig. 7 clearly puts forward a preferential degradation of the PFSA membrane in the channel regions. The membrane thickness did not significantly decrease under the lands when the anode defect was located near anode inlet (i.e. where the hydrogen concentration is the highest), while it was almost as low as under the channels when the anode defect was located near the anode outlet (i.e. where the hydrogen concentration is the lowest). Keeping in mind that the cell was fed with air and hydrogen in counter-flow mode and that inlet RH of both gases

is equal to 50%, a possible interpretation of this behavior is that the membrane thinning is, at least in this case, governed by oxygen crossover rather than hydrogen crossover.

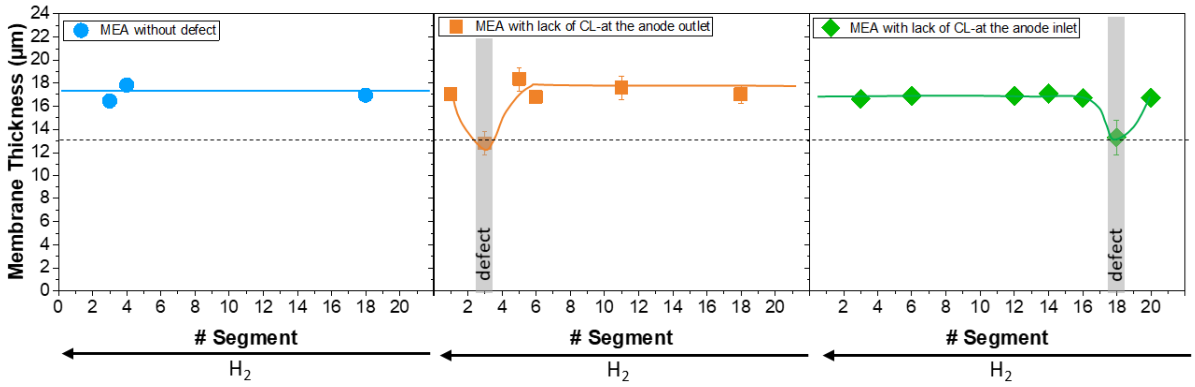

Figure 6. Overall thickness of the membrane at different segments (#18, #16, #10 or #11, #6 and #3) after 240 hours of AST. Homogeneous MEA without defect (segments #3, #4 and #18), MEA with lack of CL at the anode outlet (segments #1, #3, #5, #6, #11, #18) and at anode inlet (segments #3, #6, #12, #14, #16, #18 and #20). Ten measurements were made in the segments with a defect, *i.e*. five in the channel region and five below the lands. Only three measurements were made in the other segments because it quickly appeared that the membrane thickness was unaffected. Data plotted on the graphs correspond to the average values and the error bars stand for the standard deviation.

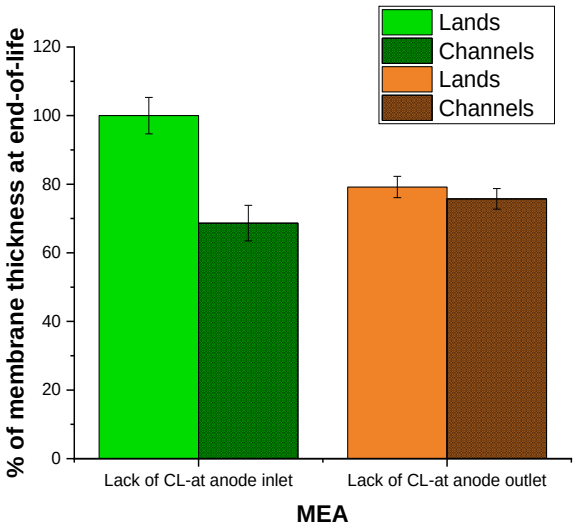

Figure 7. EoT membrane thickness compared to BoL (100%), below the channels and below the lands, in the segments with a lack of anode CL (*i.e*. #3 in the case of the MEA with a lack of anode CL near the hydrogen outlet, and #18 in the case of the MEA with a lack of anode CL near the hydrogen inlet). Data plotted on the graphs correspond to the average values of five measurements, with standard deviation.

Discussion

Impact of the anode defect

Overall, these first results clearly show an accelerated degradation of the MEA when there is a lack of anode CL in some segments, with multiple impacts on FC performances, CL and membrane's materials.

First, in term of FC voltage, the performance decay and OCV loss during the AST were always more severe with the MEA with a lack of anode CL than with the homogeneous MEA. Note that although -for clarity- only the FC voltage at 0.5 A/cm² and OCV are plotted in Fig. 4, the tendencies were similar over the whole of the polarization curves: they can be seen in Fig. S1 of Supplementary Information (SI). The performance loss seems to depend on the location of the defect, being much more significant when it is located near the hydrogen outlet. In addition, the degradation rates of the average cathode ECSA were higher in the presence of a defect than with the homogeneous MEA: about -40% loss over the test duration, *vs*. -30% with the homogeneous MEA. These values did not vary significantly with the defect location (Table 1). The design of the segmented cell does not enable to monitor the local change of cathode ECSA in the segments with a lack of anode CL. However, the degradation rates were seemingly homogeneous in the other segments (those without initial defect), and possibly linked mostly to the increase of the local current density (Fig. 5c and e).

Degradation of the anode average ECSA was also observed with the MEA with a lack of anode CL, while it improved by 21% during the AST with the homogeneous MEA. The differences were more intense than for the cathode ECSA and seem to depend on the defect location, with a faster degradation rate when it is located near the anode inlet (Table 1). Furthermore, the changes of the anode local ECSA evidenced a propagation of the defects downstream, in the direction of the hydrogen flow (Fig. 5, d and f). This propagation probably participates to the higher ECSA degradation rate when the defect is located near the hydrogen inlet.

Finally, the results evidenced a *ca*. 25% decrease in membrane thickness for the defective segments (Fig. 6). When the defect was located near the hydrogen inlet, the thinning was much more pronounced in the channels than under the lands; in opposition, the thinning was quite homogeneous when the defect was located near the hydrogen outlet (Fig. 7). Contrary to what was put forward with the anode local ECSA, no evidence of defect propagation was found. However, one cannot exclude that propagation would eventually happen with longer duration AST. Longer duration AST may also induce an increase of the hydrogen permeation currents due to excessive membrane thinning, but this was not observed here (Fig. 4).

Local electrode potentials

Given that this work made possible to establish a clear link between -intentionally prepared- anode defects and membrane thinning, it may be interesting to relate these results to those of

Sompalli et al. [37], who observed membrane degradation in the regions where the cathode overlaps the anode upon an accelerated membrane durability test protocol. According to them, this phenomenon was rationalized by the high potential occurring in this region in conjunction with the reported accelerated PFSA degradation at OCV conditions. However, this explanation was only supported by numerical simulations [38,39], no direct measurement of the local potentials having been performed (to our knowledge).

Since similar mechanisms may be at stake in our case, local potentials were monitored during the AST using the reference hydrogen electrodes (RHE) installed in the segmented cell (Fig. 1). Figure 8 shows the voltage (left), cathode local potentials (middle) and anode local potentials (right) as functions of (local) current density in the case of the MEA with a lack of anode CL near the hydrogen inlet (above) and near the hydrogen outlet (below). For clarity, the values measured in all the segments except the ones with the defect are plotted in black. As mentioned in the experimental section, the defect was either located (centered) on segment #18 and half of the adjacent ones (*i.e*. #17 and #19), when the defect is close to the hydrogen inlet, or on segment #3 and half of segments #2 and #4 when the defect is close to the hydrogen outlet.

The obvious conclusion that can be drawn from Figure 8 is that the lack of anode CL does not entail any cathode high potential excursion, neither in the segments with defects, nor in the other ones: the cathode potential in the segments with defects are always lower, or of the same order than those measured in the other segments. For clarity, only the data measured at BoL are plotted in Figure 8, but in this regard, no significant change occurred during the AST (Fig. S2 of SI). Thus, the membrane and ECSA degradation that were observed are not linked to any so-called “OCV conditions” or similar phenomenon, here. It must be emphasized that a lack of anode CL or *a fortiori* a severe degradation of the anode CL cannot be not equivalent to fuel starvation since hydrogen is still present in the anode compartment.

Figure 8 also shows a difference in behavior of the anode and cathode local potentials between the two MEA. On the one hand (above, defect near the hydrogen inlet), one can observe local cathode potentials being lower in the defective segments than in the others, while the local anode potentials remain unaffected. On the other hand (below, defect near the hydrogen outlet), the local cathode potentials in the defective segments remain close to the values reached in the other segments, while the anode local potentials increase significantly in the

segments with defect. Before trying to interpret this difference, it may be worth clarifying the meaning of “anode local potentials” in the absence of anode CL.

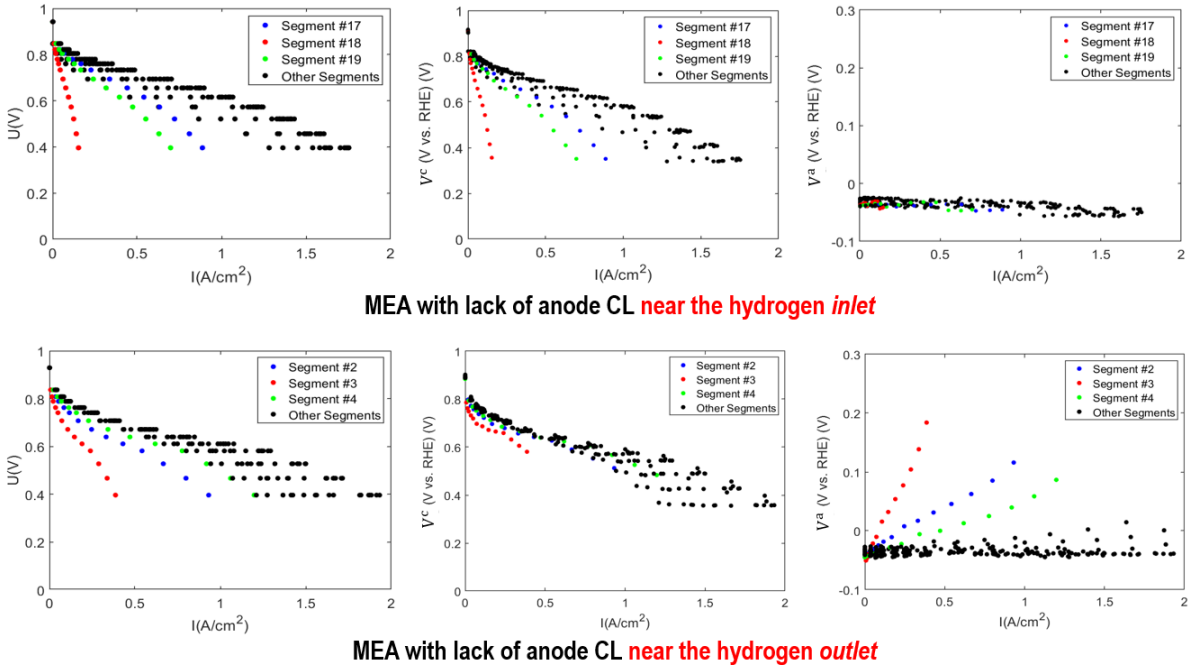

Figure 8. Local polarization curves (left), cathode local potentials (middle) and anode local potentials (right) as functions of the current density in the case of the MEA with a lack of anode CL near the hydrogen inlet (above) and near the hydrogen outlet (below). All data are plotted in black, except those measured in the segments with defect. The defect was either centered on segment #18 or on segment #3 and spread to half the area of the adjacent segments. The dots appear horizontally aligned on the polarization curves because all segments are electrically connected in parallel once the local currents - which vary from one segment to the other- are measured.

First, it must be kept in mind that although the RHE are located on the cathode side, the electrolyte potential they measure is governed by the shortest distance to the anode or cathode: if both electrodes were perfectly facing each other, then $V_e(i)$ would be equal to $\frac{V_e^a(i)+V_e^c(i)}{2}$, with $V_e^a(i)$ and $V_e^c(i)$ denoting the electrolyte potential at the anode and cathode interface, respectively, in segment #i. If the RHE is closer to the anode, because of a possible misalignment of the electrodes, then $V_e(i) \approx V_e^a(i)$, while $V_e(i) \approx V_e^c(i)$ if the RHE is closer to the cathode. This result has been shown several times through numerical simulations [39,83]: according to Liu et al. [39], $V_e(i) \approx V_e^a(i)$ and $V_e(i) \approx V_e^c(i)$ can be considered as valid assumptions when the misalignment between the anode and cathode and the distance of the reference electrodes from the closest MEA edge are both higher than 150% of the membrane thickness (*i.e.* about 30 µm in our case). In other words, what is denoted as the anode potential

in Figure 8 is equal to $V_m^a - V_e(i)$, with V_m^a the anode plate potential, and $V_e(i)$ the electrolyte potential *right below the RHE*.

In the segments without defect, $V_e^c(i) < V_e(i) < V_e^a(i)$, the exact value of $V_e(i)$ being governed by both the RHE distance from the MEA edge, and the misalignment of the anode and cathode. Nevertheless, as mentioned in the experimental section, the difference between $V_e^c(i)$ and $V_e^a(i)$ is expected to be at most of the order of a few tenths of mV due to the membrane very small thickness and resistance.

In the segments with defect, in the absence of an anode CL, it seems reasonable to expect that the membrane local potential is governed by the cathode, so that $V_e(i) \approx V_e^c(i)$. The difference between $V_e^c(i)$ and $V_e^a(i)$ is still expected to be small, first because the local current densities are low due to the absence of anode CL (see the polarization curves in Figure 8, left), second because there is no reason to expect a severe membrane dehydration (*i.e*. a large increase of its local resistance) in these regions, the membrane being still in contact with wet gases: $V_e^a(i) \approx V_e(i) \approx V_e^c(i)$. As a result, the anode potential in Figure 8 is probably still *equal or close to* $V^a(i) = V_m^a - V_e^a(i)$ (1), in the segments with a lack of anode CL, keeping in mind that V_m^a is assumed uniform over the whole of the anode plate because of its high electrical conductivity. The increase of the local membrane potential that is observed in Figure 8 (right) in the case of the MEA with a lack of anode CL near the hydrogen outlet may thus be due to oxygen crossover through the membrane.

Conversely, Figure 8 shows no increase of local anode (electrolyte) potential in the case of the MEA with a lack of anode CL near the hydrogen inlet. Nevertheless, this result is the only one presented in this work that could not be repeated yet and should therefore be considered with care. It could be explained by the lower oxygen partial pressure near the outlet of the cathode compartment since the cell was fed with air and hydrogen in counter-flow. This is consistent with the heterogeneous membrane degradation observed in this region, with no thinning observed under the lands; the membrane thinning was more homogeneous when the defect was close to the hydrogen outlet.

Finally, one cannot totally exclude that the difference in the variations of the local potentials observed in Figure 8 as functions of the location of the defect can be due to some experimental artifact(s). Further experiments and possibly numerical simulations will be necessary to confirm

the interpretation we are proposing. Nevertheless, complementary measurements were already performed with other MEA in different conditions (BoL, EoT, …) and they all confirmed an absence of high potential excursion at the cathode, or so-called “OCV conditions”: the membrane accelerated degradation that was observed in the absence of anode CL is therefore more likely explained by chemical mechanisms (*i.e.* gas crossover [50]) rather than electrochemical mechanisms (*i.e*. high potentials).

Degradation mechanisms

In view of these results on electrode potentials, some additional comments can be made regarding the impact of anode defects on MEA degradation mechanisms.

First of all, in the absence of high potential excursion, the decrease of the cathode ECSA has to be attributed mainly to potential cycling, leading to carbon corrosion, Pt migration and agglomeration, as well as Pt particles dissolution and redeposition, as widely discussed in the literature [9–13,84]. There is a fairly broad consensus on these mechanisms, although some discussions may remain open on certain points, like the impact of RH: Borup et al. [14] reported for instance a decrease in carbon corrosion with an increase in humidity during potential cycling while Nikkuni et al. observed the opposite [15]. In this study however, the AST included load-induced HR cycling, known to have an accelerating effect on the CL microstructure degradation [69,70,81,85,86]. It must also be noted that elevated temperature is usually considered an aggravating factor for CL degradation [16,87,88], which may be the main reason why higher rates of decrease of the average cathode ECSA are observed in the presence of defects: higher local currents probably translate into higher electrode temperature.

The AST (Figure 3) that was applied to the MEA was also designed to stress the membrane through humidity cycling and OCV hold sequences. As mentioned in the introduction, membrane aging mechanisms are governed by the mechanical and chemical stresses it undergoes during FC operation [41–47], and AST like this one ultimately lead to an increase of hydrogen crossover -evidenced for instance through the hydrogen permeation currents- and membrane failure [22,42]. In the present case, the AST was stopped before any noticeable increase of the hydrogen permeation current, but a significant thinning of membrane was however observed for the defective segments (Fig. 6). These results are consistent with those of Tavassoli et al. [79], who found that anode CL delamination can accelerate local membrane thinning. Such a decrease of the membrane thickness has to be linked to a local increase of

the chemical stress, which could be explained by more significant gas crossover, and/or a higher impact of gas crossover (*i.e*. more hydrogen peroxide production), in the absence of anode CL. The results of the previous section clearly show that high local potential excursions or so-called “OCV conditions” *are not* the origin of membrane thinning. It must also be noted that the MEA were made using composite Gore 735.18 membranes including Pt particles in the external layer, on the cathode side. In the absence of clear consensus in the literature regarding the impact of Pt particles on the membrane degradation rate [50,89], our future works will focus on this point. Indeed, some authors suggest that the Pt band resulting from long-range Ostwald ripening could promote the formation of radicals due to possible Fenton-like reaction [40,58,90,91], while some others believe that the Pt band may improve the membrane durability by decomposing hydrogen peroxide (H_2O_2) into oxygen and water [92–95]. Finally, heterogeneous degradations of the membrane were already reported in the literature, although in very different conditions [96]. In the present case, the membrane seems more degraded when the defect is located near the air inlet than when it is located near the hydrogen inlet, with a thinning spreading below the lands. This difference may be explained by the higher oxygen partial pressure in the region, leading to more significant oxygen crossover toward the anode, and thus hydrogen peroxide formation.

Although rarely discussed in the literature, anode degradation was already reported, in various conditions, including this specific AST in a previous work [20–23]. As mentioned earlier, the monitoring of local anode potentials showed that carbon corrosion cannot thermodynamically occur (or at a very low rate) in such conditions, including during transients. The loss of anode ECSA is therefore -and most probably- not due to classical Pt particles detachment induced by the corrosion of the carbon support. Other explanation than potential cycling must be considered, like a possible mechanical destabilization of the anode microstructure under wet-dry cycling, which has already been reported in the case of *in situ* and *ex situ* experiments [69,70,85]. The elevation of temperature at high current density, known to entail local membrane dehydration (whatever the gas inlet RH) [87] may also be one of the factors governing anode aging. The main finding of this work is probably the propagation of the anode defects, resulting in higher anode ECSA degradation rates, in the neighboring segments, downstream in the direction of the hydrogen flow (Fig. 5, d and f). Further work will be necessary to better describe

and fully understand the phenomena governing this defect propagation. For the time being, one can only -carefully- suppose that it does not rely on electrochemical mechanisms.

Conclusion

The impact and propagation of anode defects taking the form of a lack of CL was investigated using an AST combining potential and humidity cycles, and OCV holds. Customized MEA were intentionally prepared with anode defects close to the hydrogen inlet or outlet. The measurements were performed using a segmented and instrumented cell, making it possible to follow how the local performances varied and to track the anode and cathode local ECSA. The results were compared to those of a reference MEA, without defects.

The results clearly showed an accelerated degradation of the MEA when there is a lack of anode CL in some segments, with multiple impacts on FC performance, and electrode CL and membrane degradations. The results also suggest that *in term of anode ECSA*, the anode defect may propagate in the direction of hydrogen flow. The cathode ECSA was also impacted, although seemingly homogeneously. A significant membrane thinning was observed in the defective segments, without significant propagation to the adjacent ones. However, one cannot exclude, that propagation would happen for longer AST, especially considering the degradation of the anode CL in the direction of the hydrogen flow. This point will be the subject of future work.

The monitoring of anode and cathode local potential during the AST did not reveal any excursion of the cathode potential to abnormally high values, neither in the defective segments nor in the others. This allowed to propose some initial interpretations of the results, which will have to be confirmed by additional post-mortem analyses: in particular, the membrane and anode CL accelerated degradation is more likely governed by chemical mechanisms (*i.e*. gas crossover) than by electrochemical mechanisms (*i.e.* high potentials).

Acknowledgements

This work was partially funded by the French National Research Agency project LOCALI (ANR-17-CE05-0016) and by the French Environmental and Energy Management Agency (ADEME).

References

1. Wang, M. *et al.* Visualization, understanding, and mitigation of process-induced-membrane irregularities in gas diffusion electrode-based polymer electrolyte

membrane fuel cells. *Int. J. Hydrogen Energy* **46**, 14699–14712 (2021).

2. Lim, C. *et al.* Membrane degradation during combined chemical and mechanical accelerated stress testing of polymer electrolyte fuel cells. *J. Power Sources* **257**, 102–110 (2014).

3. Xinyu, H. et al. Mechanical Endurance of Polymer Electrolyte Membrane and PEM Fuel Cell Durability. *Wiley Intersci.* 2346–2357 (2006) doi:10.1002/polb.

4. Kim, S., Ahn, B. K. & Mench, M. M. Physical degradation of membrane electrode assemblies undergoing freeze/thaw cycling: Diffusion media effects. *J. Power Sources* **179**, 140–146 (2008).

5. Venkatesan, S. V., Dutta, M. & Kjeang, E. Mesoscopic degradation effects of voltage cycled cathode catalyst layers in polymer electrolyte fuel cells. *Electrochem. commun.* **72**, 15–18 (2016).

6. Guilminot, E. *et al.* Membrane and Active Layer Degradation upon PEMFC Steady-State Operation. *J. Electrochem. Soc.* **154**, B1106 (2007).

7. Chung, C. G., Kim, L., Sung, Y. W., Lee, J. & Chung, J. S. Degradation mechanism of electrocatalyst during long-term operation of PEMFC. *Int. J. Hydrogen Energy* **34**, 8974–8981 (2009).

8. Wang, X., Kumar, R. & Myers, D. J. Effect of voltage on platinum dissolution relevance to polymer electrolyte fuel cells. *Electrochem. Solid-State Lett.* **9**, 225–228 (2006).

9. Borup, R. *et al.* Scientific aspects of polymer electrolyte fuel cell durability and degradation. *Chem. Rev.* **107**, 3904–3951 (2007).

10. Wang, C. *et al.* Improved Carbon Corrosion and Platinum Dissolution Durability in Automotive Fuel Cell Startup and Shutdown Operation. *J. Electrochem. Soc.* **168**, 034503 (2021).

11. Ren, P. *et al.* Degradation mechanisms of proton exchange membrane fuel cell under typical automotive operating conditions. *Prog. Energy Combust. Sci.* **80**, 100859 (2020).

12. Okonkwo, P. C. *et al.* Platinum degradation mechanisms in proton exchange membrane fuel cell (PEMFC) system: A review. *Int. J. Hydrogen Energy* **46**, 15850–15865 (2021).

13. Sasaki, K., Shao, M. & Adzic, R. Dissolution and stabilization of platinum in oxygen cathodes. *Polym. Electrolyte Fuel Cell Durab.* 7–27 (2009) doi:10.1007/978-0-387-85536-3_2.

14. Borup, R. L., Davey, J. R., Garzon, F. H., Wood, D. L. & Inbody, M. A. PEM fuel cell electrocatalyst durability measurements. *J. Power Sources* **163**, 76–81 (2006).

15. Nikkuni, F. R. *et al.* The role of water in the degradation of Pt3Co/C nanoparticles: An Identical Location Transmission Electron Microscopy study in polymer electrolyte environment. *Appl. Catal. B Environ.* **156**–**157**, 301–306 (2014).

16. Bi, W. & Fuller, T. F. Temperature Effects on PEM Fuel Cells Pt/C Catalyst Degradation. *J. Electrochem. Soc.* **155**, B215 (2008).

17. Bi, W., Sun, Q., Deng, Y. & Fuller, T. F. The effect of humidity and oxygen partial pressure on degradation of Pt/C catalyst in PEM fuel cell. *Electrochim. Acta* **54**, 1826–1833 (2009).

18. Al-Othman, A. *et al.* The effect of glycerol on the conductivity of Nafion-free ZrP/PTFE composite membrane electrolytes for direct hydrocarbon fuel cells. *J. Power Sources*

199, 14–21 (2012).

19. Al-Othman, A. *et al.* Novel composite membrane based on zirconium phosphate-ionic liquids for high temperature PEM fuel cells. *Int. J. Hydrogen Energy* **46**, 6100–6109 (2021).

20. Schwämmlein, J. N., Rheinländer, P. J., Chen, Y., Freyer, K. T. & Gasteiger, H. A. Anode Aging during PEMFC Start-Up and Shut-Down: H 2 -Air Fronts vs Voltage Cycles . *J. Electrochem. Soc.* **165**, F1312–F1322 (2018).

21. Kim, J., Kim, M., Lee, B. G. & Sohn, Y. J. Durability of high temperature polymer electrolyte membrane fuel cells in daily based start/stop operation mode using reformed gas. *Int. J. Hydrogen Energy* **40**, 7769–7776 (2015).

22. Touhami, S. *et al.* Anode aging in polymer electrolyte membrane fuel Cells I: Anode monitoring by ElectroChemical impedance spectroscopy. *J. Power Sources* **481**, (2021).

23. Kim, M. *et al.* Effects of anode flooding on the performance degradation of polymer electrolyte membrane fuel cells. *J. Power Sources* **266**, 332–340 (2014).

24. Wagner, N. & Gülzow, E. Change of electrochemical impedance spectra (EIS) with time during CO-poisoning of the Pt-anode in a membrane fuel cell. *J. Power Sources* **127**, 341–347 (2004).

25. Ciureanu, M. Electrochemical Impedance Study of Electrode-Membrane Assemblies in PEM Fuel Cells: I. Electro-oxidation of H[sub 2] and H[sub 2]/CO Mixtures on Pt-Based Gas-Diffusion Electrodes. *J. Electrochem. Soc.* **146**, 4031 (1999).

26. Profatilova, I., Jacques, P.-A. & Escribano, S. Evaluation of Parameters Accelerating the Aging of PEMFCs Operating under Reformate Containing Carbon Monoxide. *J. Electrochem. Soc.* **165**, F3251–F3260 (2018).

27. Le Canut, J.-M., Abouatallah, R. M. & Harrington, D. A. Detection of Membrane Drying, Fuel Cell Flooding, and Anode Catalyst Poisoning on PEMFC Stacks by Electrochemical Impedance Spectroscopy. *J. Electrochem. Soc.* **153**, A857 (2006).

28. Nakajima, H., Konomi, T., Kitahara, T. & Tachibana, H. Electrochemical impedance parameters for the diagnosis of a polymer electrolyte fuel cell poisoned by carbon monoxide in reformed hydrogen fuel. *J. Fuel Cell Sci. Technol.* **5**, 1–6 (2008).

29. Reiser, C. A. *et al.* A reverse-current decay mechanism for fuel cells. *Electrochem. Solid-State Lett.* **8**, 273–276 (2005).

30. Durst, J. *et al.* Degradation heterogeneities induced by repetitive start/stop events in proton exchange membrane fuel cell: Inlet vs. outlet and channel vs. land. *Appl. Catal. B Environ.* **138**–**139**, 416–426 (2013).

31. Dillet, J. *et al.* Impact of flow rates and electrode specifications on degradations during repeated startups and shutdowns in polymer-electrolyte membrane fuel cells. *J. Power Sources* **250**, 68–79 (2014).

32. Brightman, E. & Hinds, G. In situ mapping of potential transients during start-up and shut-down of a polymer electrolyte membrane fuel cell. *J. Power Sources* **267**, 160–170 (2014).

33. Lamibrac, A. *et al.* Experimental characterization of internal currents during the start-up of a proton exchange membrane fuel cell. *J. Power Sources* **196**, 9451–9458 (2011).

34. Lamibrac, A. *et al.* Local degradations resulting from repeated start-ups and shutdowns in Proton Exchange Membrane Fuel Cell (PEMFC). *Energy Procedia* **29**,

318–324 (2012).

35. Abbou, S., Dillet, J., Maranzana, G., Didierjean, S. & Lottin, O. Local potential evolutions during proton exchange membrane fuel cell operation with dead-ended anode – Part I: Impact of water diffusion and nitrogen crossover. *J. Power Sources* **340**, 337–346 (2017).

36. Abbou, S., Dillet, J., Maranzana, G., Didierjean, S. & Lottin, O. Local potential evolutions during proton exchange membrane fuel cell operation with dead-ended anode – Part II: Aging mitigation strategies based on water management and nitrogen crossover. *J. Power Sources* **340**, 419–427 (2017).

37. Sompalli, B., Litteer, B. A., Gu, W. & Gasteiger, H. A. Membrane Degradation at Catalyst Layer Edges in PEMFC MEAs. *J. Electrochem. Soc.* **154**, B1349 (2007).

38. Adler, S. B., Henderson, B. T., Wilson, M. A., Taylor, D. M. & Richards, R. E. Reference electrode placement and seals in electrochemical oxygen generators. *Solid State Ionics* **134**, 35–42 (2000).

39. Liu, Z., Wainright, J. S., Huang, W. & Savinell, R. F. Positioning the reference electrode in proton exchange membrane fuel cells: Calculations of primary and secondary current distribution. *Electrochim. Acta* **49**, 923–935 (2004).

40. Ohma, A., Yamamoto, S. & Shinohara, K. Membrane degradation mechanism during open-circuit voltage hold test. *J. Power Sources* **182**, 39–47 (2008).

41. Subianto, S. *et al.* Physical and chemical modification routes leading to improved mechanical properties of perfluorosulfonic acid membranes for PEM fuel cells. *J. Power Sources* **233**, 216–230 (2013).

42. Lai, Y.-H. *et al.* Accelerated Stress Testing of Fuel Cell Membranes Subjected to Combined Mechanical/Chemical Stressors and Cerium Migration. *J. Electrochem. Soc.* **165**, F3217–F3229 (2018).

43. Mukundan, R. *et al.* Membrane Accelerated Stress Test Development for Polymer Electrolyte Fuel Cell Durability Validated Using Field and Drive Cycle Testing. *J. Electrochem. Soc.* **165**, F3085–F3093 (2018).

44. Robert, M. *et al.* The impact of chemical-mechanical ex situ aging on PFSA membranes for fuel cells. *Membranes (Basel).* **11**, (2021).

45. Zatoń, M., Rozière, J. & Jones, D. J. Current understanding of chemical degradation mechanisms of perfluorosulfonic acid membranes and their mitigation strategies: A review. *Sustain. Energy Fuels* **1**, 409–438 (2017).

46. Robert, M. *et al.* Effects of conjoint mechanical and chemical stress on perfluorosulfonic-acid membranes for fuel cells. *J. Power Sources* **476**, (2020).

47. Robert, M., El Kaddouri, A., Perrin, J. C., Raya, J. & Lottin, O. Time-resolved monitoring of composite Nafion™ XL membrane degradation induced by Fenton's reaction. *J. Memb. Sci.* **621**, (2021).

48. Kusoglu, A. & Weber, A. Z. A Mechanistic Model for Pinhole Growth in Fuel-Cell Membranes during Cyclic Loads. *J. Electrochem. Soc.* **161**, E3311–E3322 (2014).

49. Gubler, L., Dockheer, S. M. & Koppenol, W. H. Radical (HO●, H● and HOO●) Formation and Ionomer Degradation in Polymer Electrolyte Fuel Cells. *J. Electrochem. Soc.* **158**, B755 (2011).

50. Rodgers, M. P., Bonville, L. J., Kunz, H. R., Slattery, D. K. & Fenton, J. M. Fuel cell perfluorinated sulfonic acid membrane degradation correlating accelerated stress testing and lifetime. *Chem. Rev.* **112**, 6075–6103 (2012).

51. Frühwirt, P., Kregar, A., Törring, J. T., Katrašnik, T. & Gescheidt, G. Holistic approach to chemical degradation of Nafion membranes in fuel cells: Modelling and predictions. *Phys. Chem. Chem. Phys.* **22**, 5647–5666 (2020).

52. Gaumont, T. *et al.* Measurement of protonic resistance of catalyst layers as a tool for degradation monitoring. *Int. J. Hydrogen Energy* **42**, 1800–1812 (2017).

53. El Kaddouri, A., Flandin, L. & Bas, C. Chemical degradation of PFSA ionomer binder in PEMFC's catalyst layer. *Int. J. Hydrogen Energy* **43**, 15386–15397 (2018).

54. Felix N. Büchi, Minoru Inaba,Thomas J. Schmidt. *Polymer Electrolyte Fuel Cell Durability*. vol. 210 (2009).

55. Kitazawa, M., Nosaka, A. Y. & Nosaka, Y. Radical formation in polymer electrolyte fuel cell components as studied by ESR spectroscopy. *J. Appl. Electrochem.* **38**, 491–496 (2008).

56. Nosaka, Y., Ohtaka, K., Kitazawa, M., Kishioka, S. & Nosaka, A. Y. Spin-Trapping ESR Detection of OH Radicals Generated in the Electrode Reactions for PEFCs. *Electrochem. Solid-State Lett.* **12**, B14 (2009).

57. Ohguri, N., Nosaka, A. Y. & Nosaka, Y. Detection of OH radicals formed at PEFC electrodes by means of a fluorescence probe. *Electrochem. Solid-State Lett.* **12**, 94–96 (2009).

58. Ghassemzadeh, L., Kreuer, K. D., Maier, J. & Müller, K. Chemical degradation of Nafion membranes under mimic fuel cell conditions as investigated by solid-state NMR spectroscopy. *J. Phys. Chem. C* **114**, 14635–14645 (2010).

59. Fenton, J. M. *et al.* Membrane Degradation Mechanisms and Accelerated Durability Testing of Proton Exchange Membrane Fuel Cells. *ECS Trans.* **25**, 233–247 (2009).

60. Zhao, N. *et al.* Effects of Fuel Cell Operating Conditions on Proton Exchange Membrane Durability at Open-Circuit Voltage. *Fuel Cells* **20**, 176–184 (2020).

61. Zhang, S. *et al.* Effects of open-circuit operation on membrane and catalyst layer degradation in proton exchange membrane fuel cells. *J. Power Sources* **195**, 1142–1148 (2010).

62. Lai, Y. H., Mittelsteadt, C. K., Gittleman, C. S. & Dillard, D. A. Viscoelastic stress analysis of constrained proton exchange membranes under humidity cycling. *J. Fuel Cell Sci. Technol.* **6**, 0210021–02100213 (2009).

63. Yoon, W. & Huang, X. Study of Polymer Electrolyte Membrane Degradation under OCV Hold Using Bilayer MEAs. *J. Electrochem. Soc.* **157**, B599 (2010).

64. Kusoglu, A. & Weber, A. Z. Electrochemical/Mechanical Coupling in Ion-Conducting Soft Matter. *J. Phys. Chem. Lett.* **6**, 4547–4552 (2015).

65. Luo, X., Ghassemzadeh, L. & Holdcroft, S. Effect of free radical-induced degradation on water permeation through PFSA ionomer membranes. *Int. J. Hydrogen Energy* **40**, 16714–16723 (2015).

66. Ghassemzadeh, L., Kreuer, K. D., Maier, J. & Müller, K. Evaluating chemical degradation of proton conducting perfluorosulfonic acid ionomers in a Fenton test by solid-state 19F NMR spectroscopy. *J. Power Sources* **196**, 2490–2497 (2011).

67. Kusoglu, A., Calabrese, M. & Weber, A. Z. Effect of mechanical compression on chemical degradation of Nafion membranes. *ECS Electrochem. Lett.* **3**, 33–36 (2014).

68. Kundu, S., Fowler, M. W., Simon, L. C. & Grot, S. Morphological features (defects) in fuel cell membrane electrode assemblies. *J. Power Sources* **157**, 650–656 (2006).

69. Zhao, J., Shahgaldi, S., Li, X. & Liu, Z. (Simon). Experimental Observations of Microstructure Changes in the Catalyst Layers of Proton Exchange Membrane Fuel Cells under Wet-Dry Cycles. *J. Electrochem. Soc.* **165**, F3337–F3345 (2018).

70. Chang, Y. *et al.* Effect of humidity and thermal cycling on the catalyst layer structural changes in polymer electrolyte membrane fuel cells. *Energy Convers. Manag.* **189**, 24–32 (2019).

71. Banan, R., Zu, J. & Bazylak, A. Humidity and temperature cycling effects on cracks and delaminations in PEMFCs. *Fuel Cells* **15**, 327–336 (2015).

72. Yin, Y. *et al.* Ionomer migration within PEMFC catalyst layers induced by humidity changes. *Electrochem. commun.* **109**, 106590 (2019).

73. Chede, S., Griffiths, P., Escobar, I. C. & Harris, T. A. L. Does casting method matter in filtration membranes? A comparison in performance between doctor blade and slot-die extruded polymeric membranes. *J. Appl. Polym. Sci.* **135**, 1–8 (2018).

74. Sima Didari, Zakaria Ahmad, Jaeyun Moon, Camille Cruz, T. A. L. H. The Effects of Pinholes on the Performance of Polymer Electrolyte Fuel Cells. *ECS Meet. Abstr.* (2012) doi:10.1149/ma2012-01/28/1089.

75. Singh, Y. *et al.* Tracking the evolution of mechanical degradation in fuel cell membranes using 4D in situ visualization. *J. Power Sources* **412**, 224–237 (2019).

76. Dubau, L. *et al.* A review of PEM fuel cell durability: Materials degradation, local heterogeneities of aging and possible mitigation strategies. *Wiley Interdiscip. Rev. Energy Environ.* **3**, 540–560 (2014).

77. Uchiyama, T., Kumei, H. & Yoshida, T. Catalyst layer cracks by buckling deformation of membrane electrode assemblies under humidity cycles and mitigation methods. *J. Power Sources* **238**, 403–412 (2013).

78. Phillips, A., Ulsh, M., Porter, J. & Bender, G. Utilizing a Segmented Fuel Cell to Study the Effects of Electrode Coating Irregularities on PEM Fuel Cell Initial Performance. *Fuel Cells* **17**, 288–298 (2017).

79. Tavassoli, A. *et al.* Effect of catalyst layer defects on local membrane degradation in polymer electrolyte fuel cells. *J. Power Sources* **322**, 17–25 (2016).

80. Abbou, S. *et al.* High Potential Excursions during PEM Fuel Cell Operation with Dead-Ended Anode. *J. Electrochem. Soc.* **162**, F1212–F1220 (2015).

81. Jao, T. C., Ke, S. T., Chi, P. H., Jung, G. Bin & Chan, S. H. Degradation on a PTFE/Nafion membrane electrode assembly with accelerating degradation technique. *Int. J. Hydrogen Energy* **35**, 6941–6949 (2010).

82. Marrony, M. *et al.* Durability study and lifetime prediction of baseline proton exchange membrane fuel cell under severe operating conditions. *J. Power Sources* **182**, 469–475 (2008).

83. He, W. & Nguyen, T. Van. Edge Effects on Reference Electrode Measurements in PEM Fuel Cells. *J. Electrochem. Soc.* **151**, A185 (2004).

84. Wang, K. *et al.* Effect of load-cycling amplitude on performance degradation for proton exchange membrane fuel cell. *Chinese Chem. Lett.* 1–5 (2021) doi:10.1016/j.cclet.2021.02.045.

85. Liu, J. *et al.* Mechanical degradation of catalyst layer under accelerated relative humidity cycling in a polymer electrolyte membrane fuel cell. *J. Power Sources* **512**, 230487 (2021).

86. Vengatesan, S., Fowler, M. W., Yuan, X. Z. & Wang, H. Diagnosis of MEA degradation under accelerated relative humidity cycling. *J. Power Sources* **196**, 5045–5052 (2011).

87. Ge, N. *et al.* Membrane dehydration with increasing current density at high inlet gas relative humidity in polymer electrolyte membrane fuel cells. *J. Power Sources* **422**, 163–174 (2019).

88. Dubau, L. & Maillard, F. Unveiling the crucial role of temperature on the stability of oxygen reduction reaction electrocatalysts. *Electrochem. commun.* **63**, 65–69 (2016).

89. Ferreira, P. J. *et al.* Instability of Pt/C Electrocatalysts in Proton Exchange Membrane Fuel Cells. *J. Electrochem. Soc.* **152**, A2256 (2005).

90. Zhao, D., Yi, B. L., Zhang, H. M. & Liu, M. The effect of platinum in a Nafion membrane on the durability of the membrane under fuel cell conditions. *J. Power Sources* **195**, 4606–4612 (2010).

91. Ohma, A., Suga, S., Yamamoto, S. & Shinohara, K. Membrane Degradation Behavior during Open-Circuit Voltage Hold Test. *J. Electrochem. Soc.* **154**, B757 (2007).

92. Macauley, N. *et al.* Pt Band formation enhances the stability of fuel cell membranes. *ECS Electrochem. Lett.* **2**, 2013–2016 (2013).

93. Aoki, M., Uchida, H. & Watanabe, M. Decomposition mechanism of perfluorosulfonic acid electrolyte in polymer electrolyte fuel cells. *Electrochem. commun.* **8**, 1509–1513 (2006).

94. Aoki, M., Uchida, H. & Watanabe, M. Novel evaluation method for degradation rate of polymer electrolytes in fuel cells. *Electrochem. commun.* **7**, 1434–1438 (2005).

95. Bodner, M., Cermenek, B., Rami, M. & Hacker, V. The effect of platinum electrocatalyst on membrane degradation in polymer electrolyte fuel cells. *Membranes (Basel).* **5**, 888–902 (2015).

96. De Moor, G. *et al.* Perfluorosulfonic acid membrane degradation in the hydrogen inlet region: A macroscopic approach. *Int. J. Hydrogen Energy* **41**, 483–496 (2016).

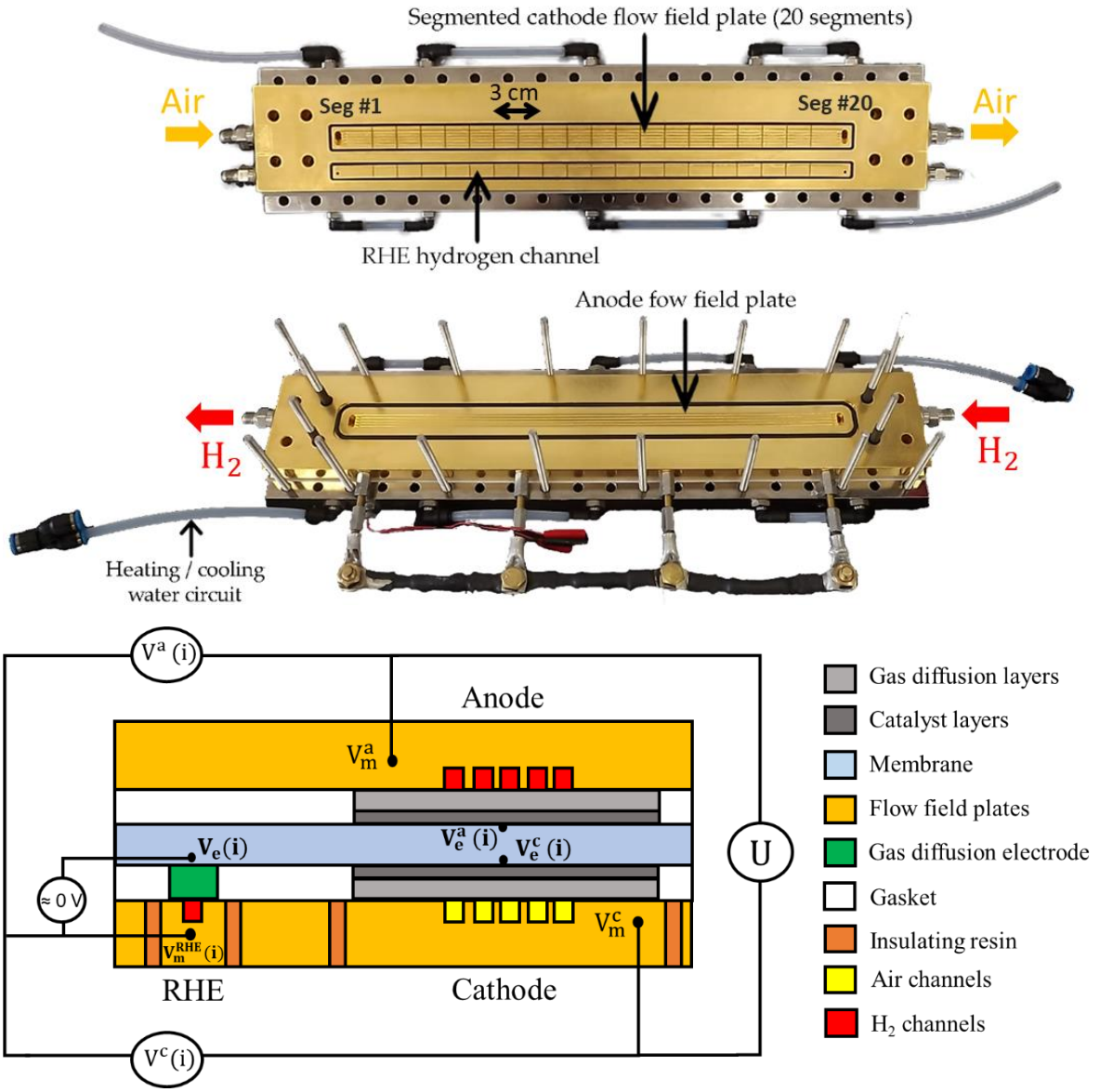

Figure 1. Pictures and operation principle of the linear segmented cell. Up: segmented cathode flow-field with the auxiliary hydrogen channel feeding the RHE used to measure the local potentials. Middle: anode flow-field plate. Bottom: cross-sectional view of the cell. The reference electrodes give access to the local electrolyte potential $V^e(i)$ and thus to the anode and cathode potentials of each segment [22,35].

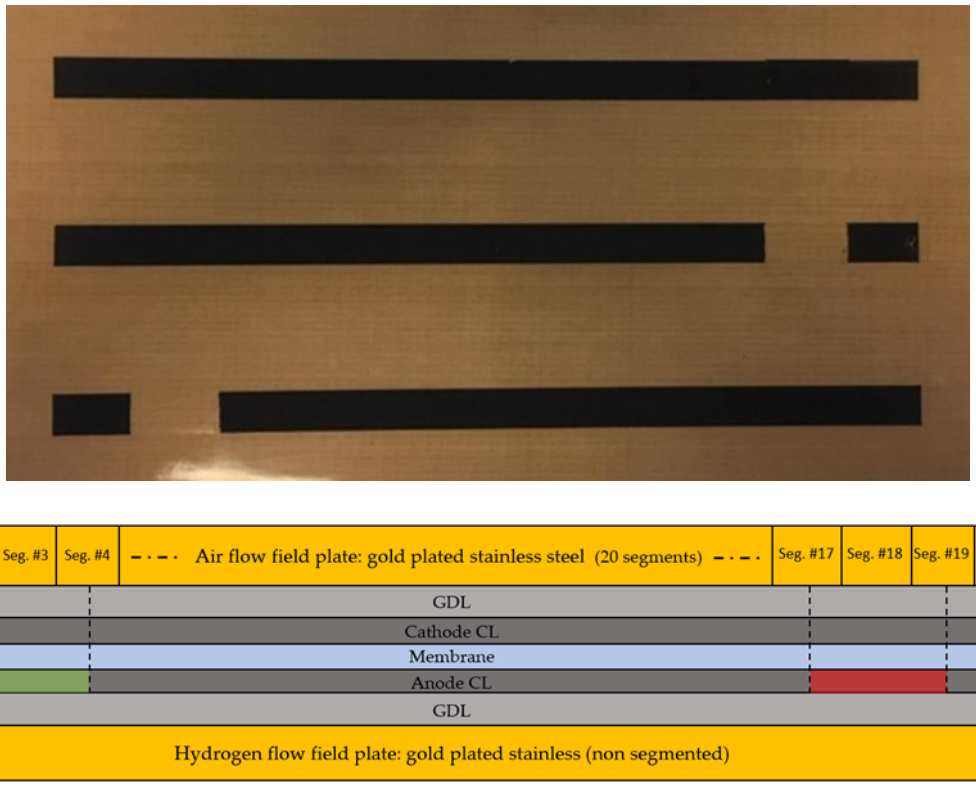

Figure 2. Up: anode -before transfer on the membrane- with -or without- a lack of CL at one end. Below: longitudinal sectional view of the segmented cell. The location of the defect is situated either at the anode inlet (in green) or outlet (in red).

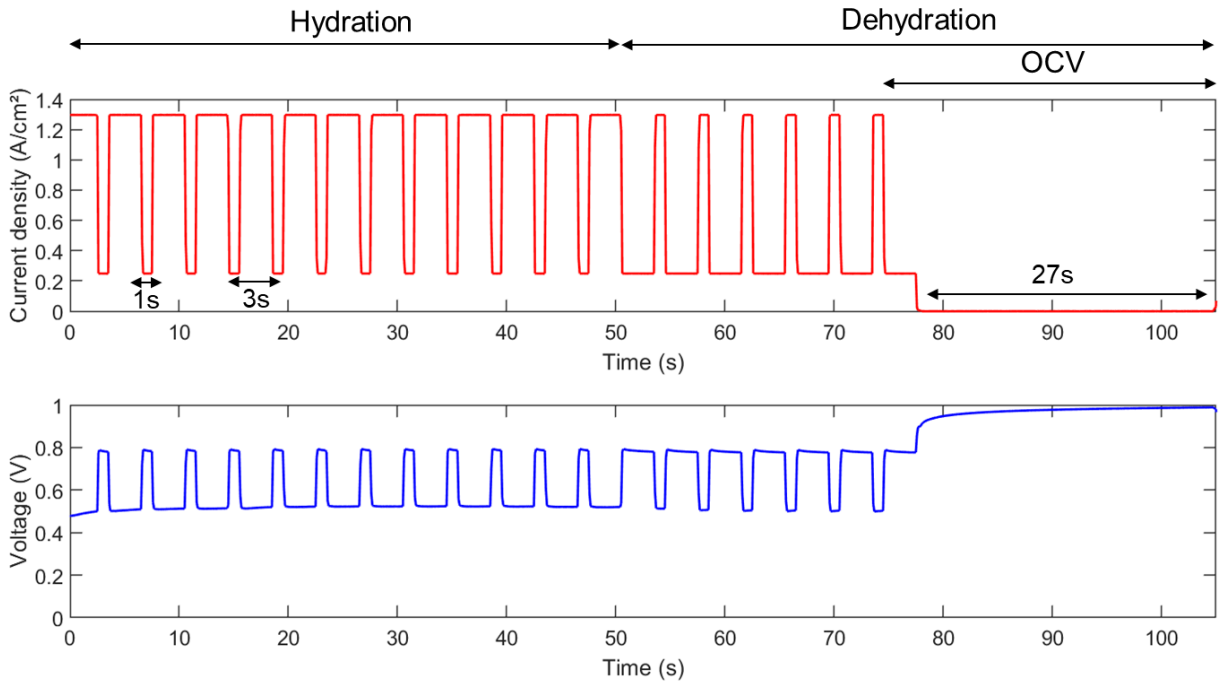

Figure 3. Current density and voltage profiles during the RH and load cycling AST. The hydration stage consists of alternating 1 s at low current (0.25 A/cm²) and 3 s at high current (1.3 A/cm²) sequences and lasts 52 s. The dehydration stage consists of alternated sequences of 3 s at low current and 1 s at high current, followed by 27 s at OCV (total duration = 105 s) [22].

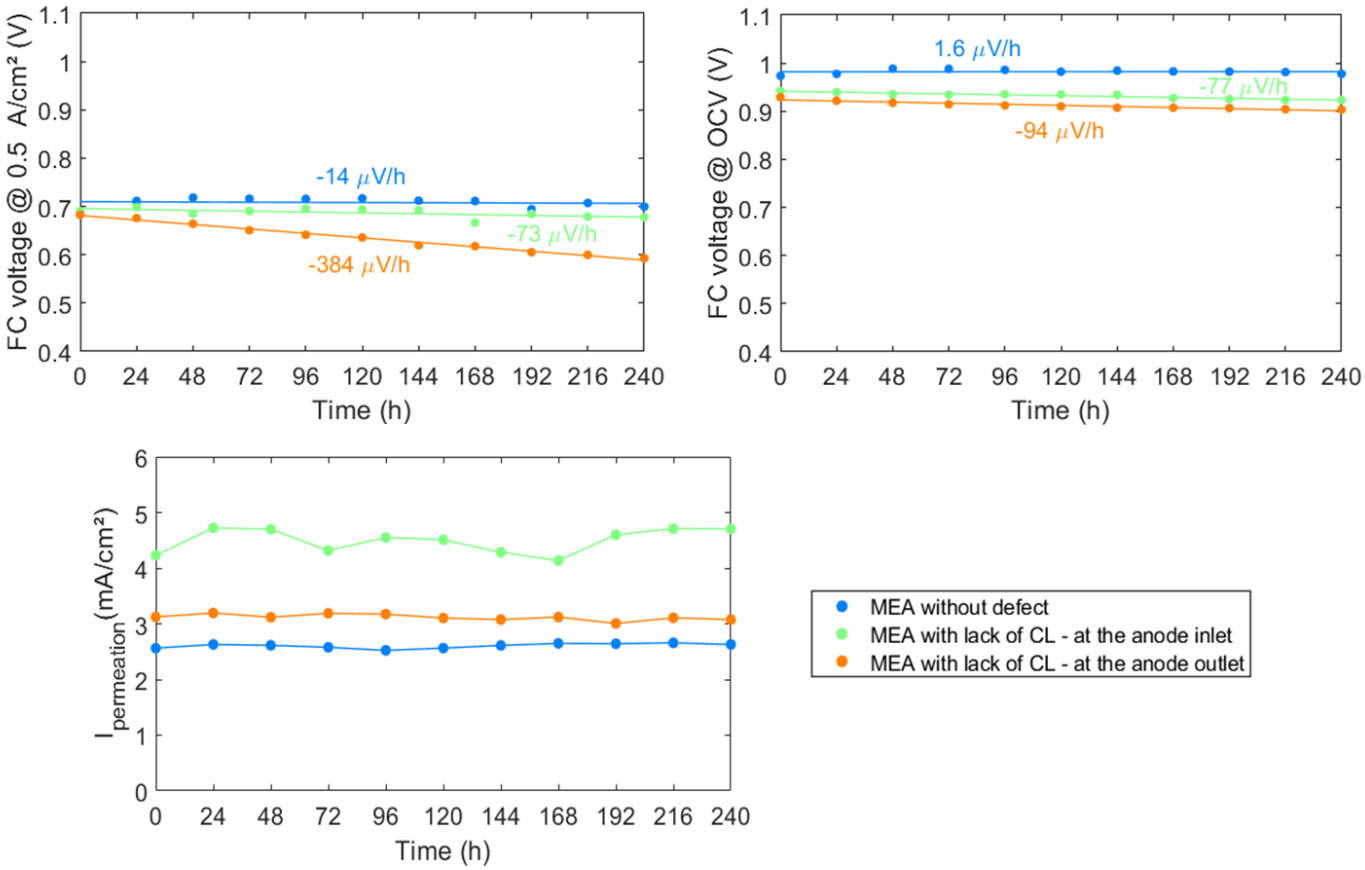

Figure 4. Variation of the FC voltage at 0.5 A/cm² (top, left), of the OCV (top, right) and of the hydrogen permeation current (bottom) during AST performed with a reference MEA (without defect), a MEA with a lack of anode catalyst layer close to the hydrogen inlet, and a MEA with a lack of anode CL close to the hydrogen outlet. All data were measured during the characterization stage performed every 24 h. The voltage degradation rates were estimated using a linear interpolation of the dots.

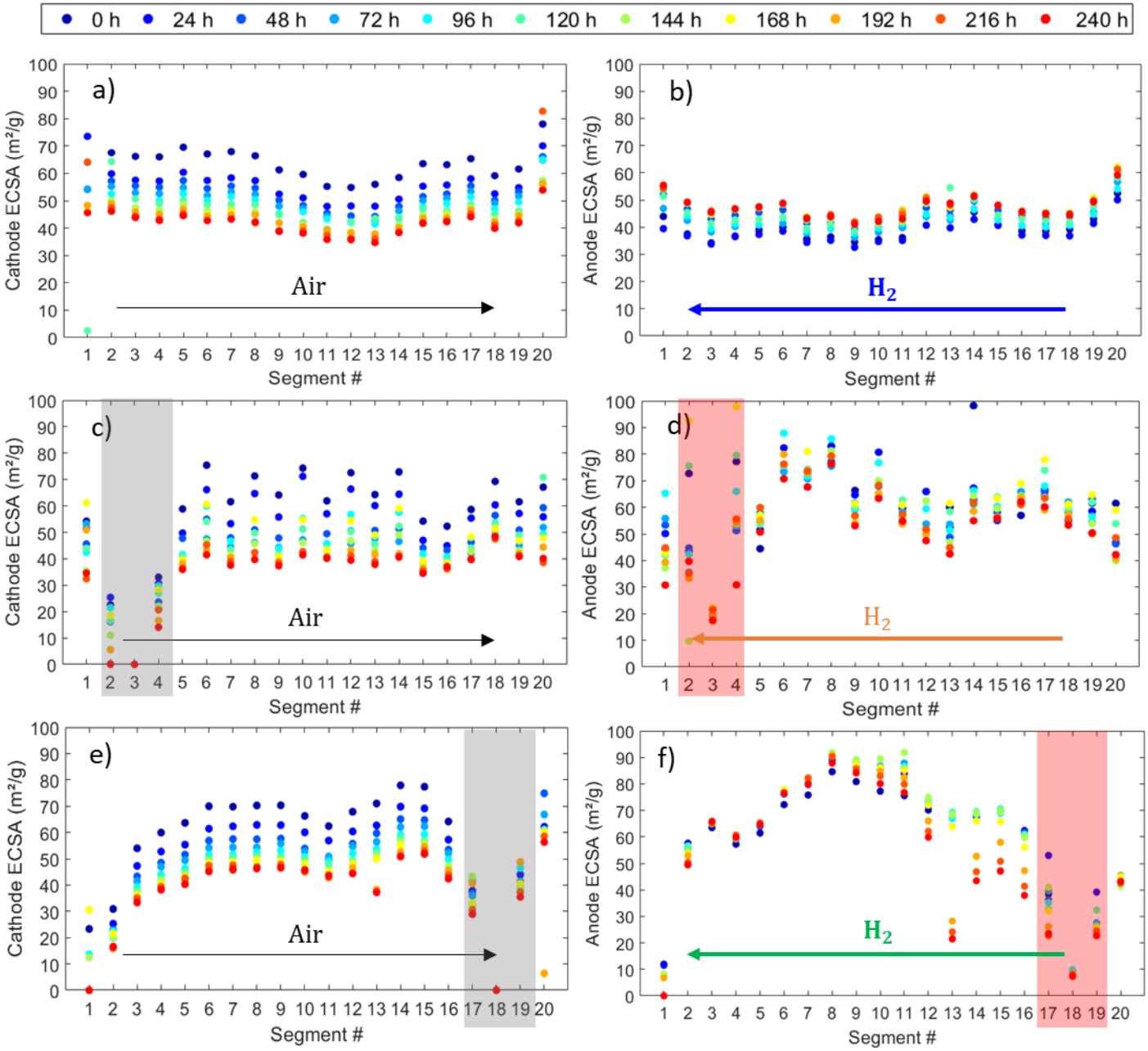

Figure 5. Variation of the local ECSA during the AST at the cathode (a, c and e) and the anode (b, d and f) in the case of the MEA without defect (a and b), the MEA with a lack of CL close to the anode outlet (c and d) and the MEA with a lack of CL close to the anode inlet (e and f), respectively. The segments corresponding to the anode defects are marked in red (d and f). The segments marked in grey are those where the cathode ECSA measurements cannot be considered as reliable due to the absence of a counter electrode.

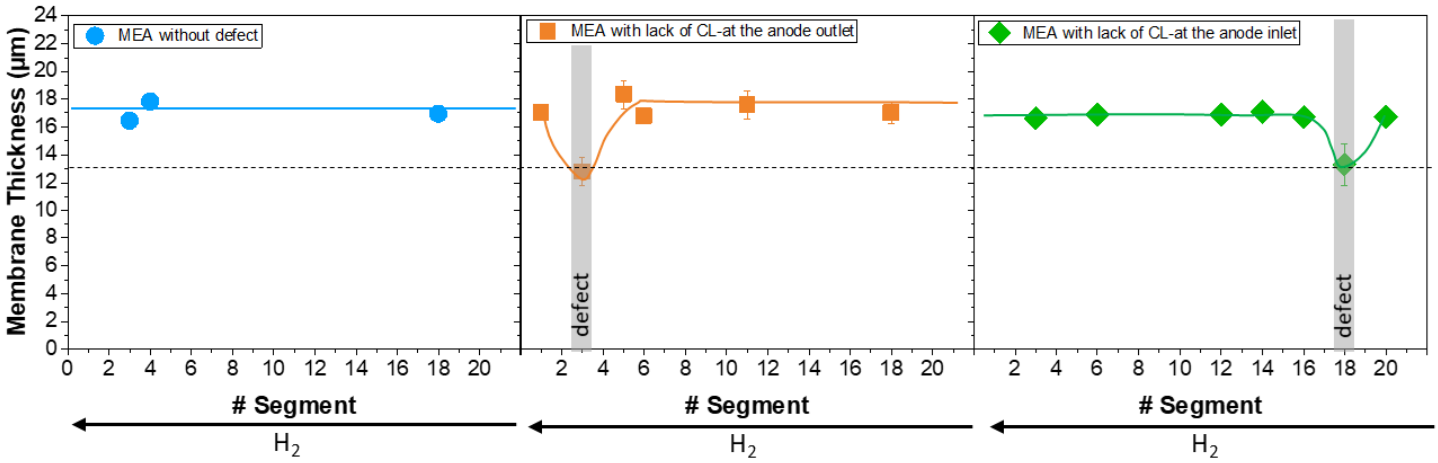

Figure 6. Overall thickness of the membrane at different segments (#18, #16, #10 or #11, #6 and #3) after 240 hours of AST. Homogeneous MEA without defect (segments #3, #4 and #18), MEA with lack of CL at the anode outlet (segments #1, #3, #5, #6, #11, #18) and at anode inlet (segments #3, #6, #12, #14, #16, #18 and #20). Ten measurements were made in the segments with a defect, *i.e*. five in the channel region and five below the lands. Only three measurements were made in the other segments because it quickly appeared that the membrane thickness was unaffected. Data plotted on the graphs correspond to the average values and the error bars stand for the standard deviation.

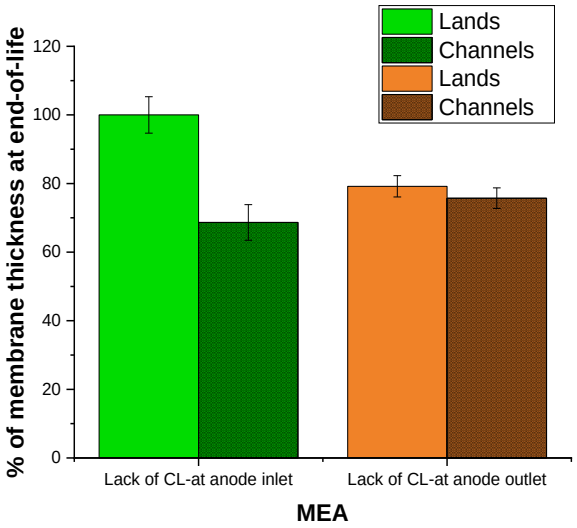

Figure 7. EoT membrane thickness compared to BoL (100%), below the channels and below the lands, in the segments with a lack of anode catalyst layer (*i.e*. #3 in the case of the MEA with a lack of anode CL near the hydrogen outlet, and #18 in the case of the MEA with a lack of anode CL near the hydrogen inlet). Data plotted on the graphs correspond to the average values of five measurements, with standard deviation.

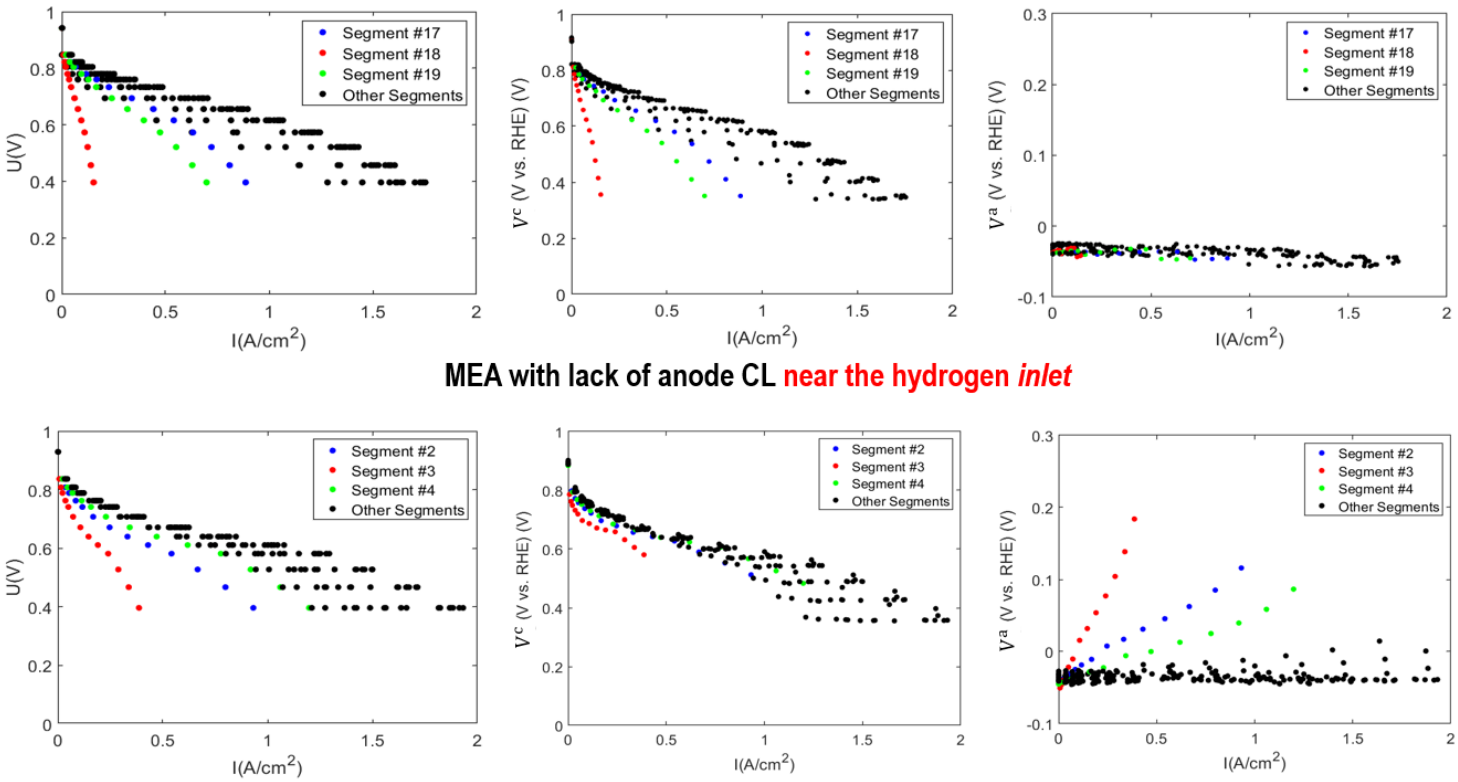

Figure 8. Local polarization curves (left), cathode local potentials (middle) and anode local potentials (right) as functions of the current density in the case of the MEA with a lack of anode CL near the hydrogen inlet (above) and near the hydrogen outlet (below). All data are plotted in black, except those measured in the segments with defect. The defect was either centered on segment #18 or on segment #3 and spread to half the area of the adjacent segments. The dots appear horizontally aligned on the polarization curves because all segments are electrically connected in parallel once the local currents - which vary from one segment to the other- are measured.

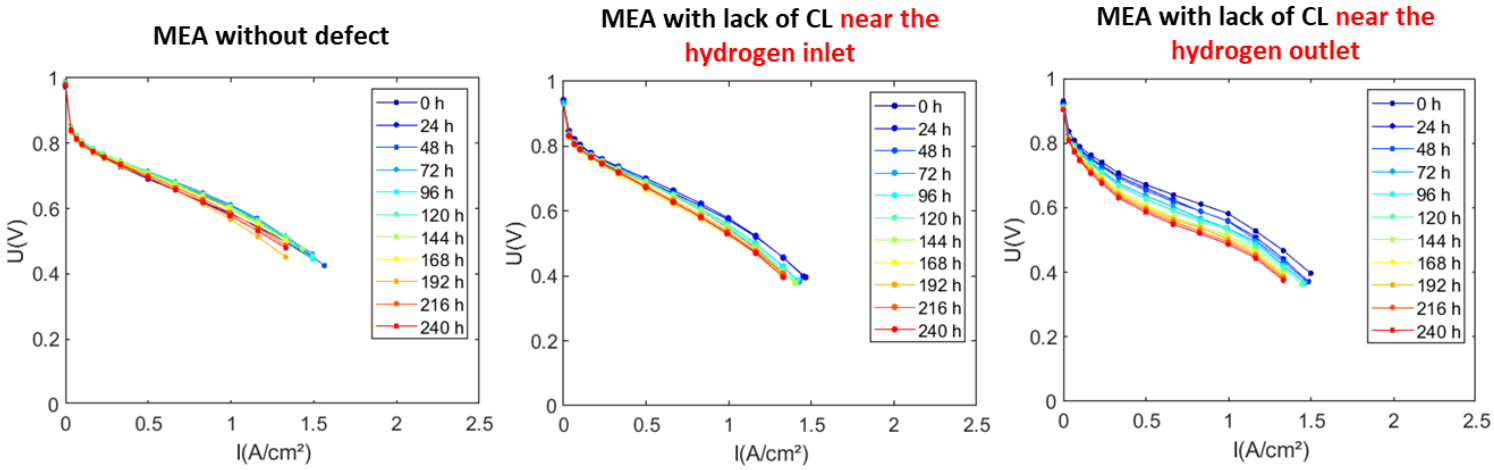

Figure S1. Polarization curves measured every 24 hours during the AST, with the MEA without defect (right), with the MEA with a lack of anode CL near the hydrogen inlet (center) and near the hydrogen outlet (right).

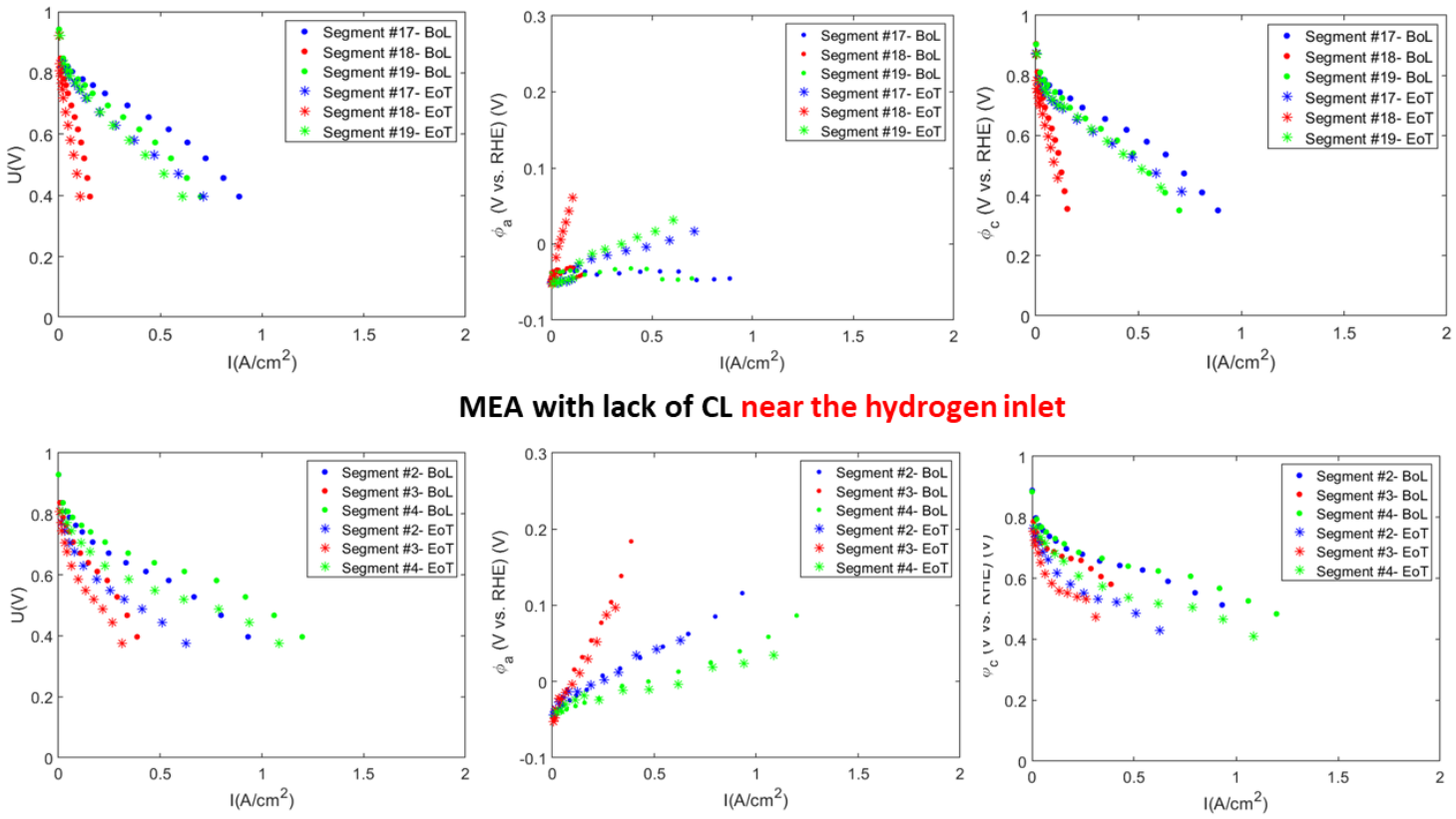

Figure S2. Local polarization curves (left), cathode local potentials (middle) and anode local potentials (right) as functions of the current density in the case of the MEA with a lack of anode CL near the hydrogen inlet (above) and near the hydrogen outlet (below). Only the data measured in the segment with defect are plotted on these graphs, at BoL and EoT.